J. Fluid Mech. (2003), *vol.* 488, *pp.* 31–78. © 2003 Cambridge University Press
DOI: 10.1017/S0022112003004786 Printed in the United Kingdom

Receptivity of a supersonic boundary layer over a flat plate. Part 1. Wave structures and interactions

By YANBAO MA AND XIAOLIN ZHONG

Mechanical and Aerospace Engineering Department, University of California,
Los Angeles, CA 90095 USA

(Received 2 February 2002 and in revised form 4 March 2003)

This paper is the first part of a two-part study on the mechanisms of the receptivity to disturbances of a Mach 4.5 flow over a flat plate by using both direct numerical simulations (DNS) and linear stability theory (LST). The main objective of the current paper is to study the linear stability characteristics of the boundary-layer wave modes and their mutual resonant interactions. The numerical solutions of both steady base flow and unsteady flow induced by forcing disturbances are obtained by using a fifth-order shock-fitting method. Meanwhile, the LST results are used to study the supersonic boundary-layer stability characteristics relevant to the receptivity study. It is found that, in addition to the conventional first and second modes, there exist a family of stable wave modes in the supersonic boundary layer. These modes play a very important role in the receptivity process of excitation of the unstable Mack modes, especially the second mode. These stable modes are termed mode I, mode II, etc., in this paper. Though mode I and mode II waves are linearly stable, they can have resonant (synchronization) interactions with both acoustic waves and the Mack-mode waves. Therefore, the stable wave modes such as mode I and mode II are critical in transferring wave energy between the acoustic waves and the unstable second mode. The effects of frequencies and wall boundary conditions for the temperature perturbations on the boundary-layer stability and receptivity are also studied.

1. Introduction

The study of laminar–turbulent transition in supersonic and hypersonic boundary layers is important to the development of future space vehicles operating at sustained supersonic and hypersonic speeds. In an environment with small initial disturbances, which is the case for most flight conditions of supersonic and hypersonic vehicles, the paths to transition can conceptually be divided into three stages: (i) receptivity, (ii) linear eigenmode growth or transient growth, and (iii) nonlinear breakdown to turbulence. The first stage, which is the receptivity process, converts the environmental disturbances into boundary-layer instability waves, such as the Tollmien–Schlichting (T-S) waves. The second stage is the linear eigenmode growth of boundary-layer instability waves, which can be obtained as the eigen-solutions of the homogeneous linearized disturbance equations. As the amplitudes of the instability waves grow, three-dimensional and nonlinear interactions occur in the form of secondary instabilities or other nonlinear interactions. Subsequent stages cause the breakdown to turbulence. The receptivity to large-amplitude free-stream disturbances may also lead to transition without the appearance of the second stage, which is called the bypass transition. In general, the transition process depends strongly on the initial flow conditions in the free stream and surface roughness at the wall.

The transition from laminar to turbulent flow in the boundary layers has been extensively studied. The most widely used transition prediction method is the semi-empirical e^N method. This method postulates that boundary-layer transition occurs when the total growth of the most unstable disturbance waves in the boundary layer exceeds some empirical factor, e^N, relative to its amplitude at the lower branch (branch I) of the neutral stability curve. The growth rates of disturbances are calculated from the linear stability theory (LST). Typical value of N, determined by comparison with experimental observations of transition locations, is between 9 and 11. The limitation of the e^N method is well known. A major drawback of the e^N method is that it does not consider the effects of free-stream disturbance environments on the onset of boundary-layer transition. Such effects can only be understood through the studies on the receptivity of boundary layers to various forcing disturbances. The receptivity mechanism provides important initial conditions of amplitude, frequency and phase for the instability waves in the boundary layers (Goldstein & Hultgren 1989). The goal of receptivity analysis is to understand the generation of instability waves for the development of transition prediction methods which take into account the effects from free-stream disturbance environments. Recent studies on receptivity are reviewed by Saric, Reed & Kerschen (2002). However, they mainly focus on receptivity of incompressible flow.

This paper is concerned with the receptivity of a supersonic boundary layer over a flat plate. The main objective of a receptivity study on a supersonic boundary layer is to investigate the mechanisms of initial generation of the unstable boundary-layer wave modes by forcing waves. The unstable wave modes in supersonic boundary layers have been identified by Mack (1984) using the LST. Because of Mack's extensive studies, the instability properties of these wave modes are currently well understood. Particularly, Mack found that there are higher acoustic instability modes in addition to the first-mode instability waves in supersonic and hypersonic boundary layers. These instability modes in supersonic boundary layers have been termed the Mack modes. Among them, the second Mack mode becomes the dominant instability mode for supersonic boundary layers at Mach numbers larger than about 4. The existence and dominance of the second mode has been validated by experimental studies (Stetson & Kimmel 1992). Experimental measurements on supersonic and hypersonic boundary-layer stability on sharp cones were performed by Kendall (1975) and others. The experimental results indicated that the first and second Mack-mode instabilities are simultaneously present in supersonic and hypersonic boundary layers. Though the linear stability of the Mack modes is well understood, it is still a subject of current research with regard to the receptivity of the supersonic boundary layer, i.e. the investigation of the mechanisms of the unstable Mack modes generated by forcing waves.

The receptivity process plays an important role in boundary-layer transition. It has been shown by experimental measurements that the transition locations (Re_T) in supersonic and hypersonic boundary layers are strongly affected by the characteristics of free-stream disturbance environments. Measurements of the transition location on a slender cone by Krogmann (1977) in a Ludwieg tube showed higher transition Reynolds numbers than those measured in other facilities with different free-stream disturbance levels. The measurements by Pate & Schueler (1969), Pate (1971), Potter & Whitfield (1962) and Potter (1968) in free-flight conditions showed that the transition Reynolds numbers increase with increasing unit Reynolds numbers of the flows, which can be attributed to the effects of free-stream disturbance environments. Stetson *et al.* (1986) studied the effects of the unit Reynolds numbers and environmental disturbances on the transition of a cone at Mach 8. They concluded that the external disturbances must be known in order to predict boundary-layer transition. Therefore, boundary-layer transition will never be successfully predicted without understanding the receptivity phenomena, i.e. how the environmental disturbances enter the boundary layers and ultimately generate boundary-layer instability waves.

Currently, the receptivity mechanisms of supersonic boundary layers to free-stream disturbances are not well understood. Even for receptivity of supersonic flow over a simple flat plate with an elliptical leading edge to free-stream disturbances, the results of receptivity experiments were difficult to interpret, often inclusive and even confusing (Reshotko 1990). This is because the non-parallel growth of the boundary layer near the leading edge, the rapid profile adjustment due to varying pressure gradients, and the change in surface curvature at the juncture of the leading edge with the flat plate, can all contribute to a source of excitation of receptivity.

There have been a few reported experimental studies on the receptivity of supersonic and hypersonic boundary layers. Maslov & Semionov (1986) and Maslov *et al.* (2001) conducted experimental investigations on the excitation of instability waves in a Mach 2 boundary layer of a flat plate by external acoustic waves emanating from another parallel flat plate below the first flat plate. They concluded that the conversion of external acoustic perturbations into the instability waves of the boundary layer on a flat plate is most intense in the following areas: the leading-edge region of the plate, the acoustic branch of the neutral stability curve, and the lower branch of the neutral stability curve. Semionov *et al.* 1996, Arnal *et al.* 1999 and Maslov *et al.* (2001) also conducted experimental investigations of hypersonic boundary-layer receptivity, on the sharp leading edge of a flat plate, to acoustic waves in a Mach 5.92 flow in the free stream. They found that acoustic waves impinging on the leading edge generate Tollmien–Schlichting waves in the boundary layer. The receptivity coefficients were obtained for several radiation conditions and intensities. It was shown that there is a dependence of receptivity coefficients on the wave inclination angles.

Most of the computational and theoretical studies on the boundary-layer receptivity have been conducted for incompressible flow (Goldstein & Hultgren 1989). There have been only a few theoretical and computational studies on the receptivity of compressible boundary layers. Mack (1975) altered his LST to include the response of compressible boundary layers to incoming acoustic waves, but the mechanism by which the forcing waves turned into boundary-layer perturbation was not considered. Choudhari & Street (1990, 1993) extended an asymptotic theory, which was successfully used in studies of subsonic receptivity (Kerschen 1989), to investigate the receptivity to localized flow inhomogeneities in a Mach 4.5 boundary layer with a zero pressure gradient. The effect of the interaction of the shock wave, which is induced by the boundary-layer displacement, with the forcing disturbances was not considered in their studies. Fedorov & Khokhlov (1991) examined the leading-edge receptivity of supersonic boundary layers to free-stream acoustic waves by an asymptotic method. It was concluded that the discrete modes of supersonic boundary layers are synchronized with acoustic waves near the leading edge. As a result of the wave synchronization, boundary-layer disturbances are strongly excited near the leading edge. Two receptivity mechanisms, diffraction and diffusion of acoustic waves on the leading edge, were proposed in their later studies (Fedorov & Khokhlov 1992). They also found that the leading-edge receptivity depends on the incident angles of the acoustic waves. Fedorov & Alexander (1997), Fedorov & Khokhlov (2001, 2002) and Fedorov & Tumin (2001) showed that strong excitation occurs when external waves and wall-induced disturbances are in resonance with the boundary-layer normal modes. Boundary-layer self-similar solutions were used in Fedorov's analyses, but the effect of the shock wave, however, was not considered.

With the development of powerful computers and advanced numerical methods, the direct numerical simulation approach of directly solving the full unsteady Navier–Stokes equations has become an important tool in the investigation of the boundary-layer receptivity process. This approach can simultaneously simulate both the effects of complex disturbance environments on boundary-layer receptivity and the shock/disturbance interactions. So far, very few numerical studies have been carried out on the supersonic and hypersonic boundary-layer receptivity. Zhong (1997, 2001) studied the receptivity of hypersonic flow over a parabola by solving full Navier–Stokes equations. The effects of bow shock interactions were accurately taken into account by using a fifth-order shock-fitting scheme (Zhong 1998). A parametric study was carried out on the receptivity characteristic for different free-stream waves, frequencies, nose bluntness characterized by Strouhal numbers, Reynolds numbers, Mach numbers and wall cooling. It was concluded that the generation of boundary-layer stability waves was mainly due to the interaction of boundary layer with the transmitted acoustic waves instead of entropy and vorticity waves. The receptivity coefficient was found to increase as the relative nose radius was decreased. Fezer & Kloker (1999) simulated receptivity of a Mach 6.8 boundary-layer flow to blowing and suction under either wind-tunnel or atmospheric conditions to investigate laminar–turbulent transition scenarios at different temperature conditions. It was found that a self-induced stabilization occurred at hot conditions for a certain disturbance level owing to strong mean-flow distortion. Lin, Malik & Sengupta (1999) and Malik (2000) studied the receptivity of a Mach 8 flow past a sharp wedge to three different types of external disturbances by solving compressible linearized Navier–Stokes equations. The forcing disturbances include: a blowing/suction embedded in the wedge surface, a narrow 'beam' of free-stream acoustic waves and plane acoustic waves in the free stream. Their results showed that similar boundary-layer instability wave patterns were obtained in all cases of different forcing disturbances.

Because of the complexity of transient supersonic flow fields involving a receptivity process with shock interaction, an effective approach to study supersonic boundary-layer receptivity is the direct numerical simulation (DNS) of the full Navier–Stokes equations. The DNS has the advantage that detailed flow characteristics of the receptivity process can be obtained with minimum simplification by using the full Navier–Stokes governing equations. Systematic numerical simulations can also be carried out to study the effects of various parameters on the receptivity characteristics. Such numerical studies can lead to an in-depth understanding of detailed flow mechanisms. So far, there are no such detailed numerical simulations on the receptivity of supersonic flow over a flat plate. The mechanisms of generation of instability wave modes inside the boundary layer are not well understood. Therefore, the objective of this paper is to study the receptivity mechanisms of the supersonic boundary layer to various forcing disturbances by using the DNS approach.

Figure 1 shows a diagram of the receptivity of a supersonic flat-plate boundary layer to free-stream disturbances. An oblique shock wave is generated in supersonic viscous flow over the flat plate owing to the displacement of the boundary layer resulting from the viscous effects. The strength of the shock is not known in advance. It depends on the free-stream Mach number and the Reynolds number of the flow. The induced oblique shock was neglected in most of the previous theoretical and computational studies of the stability and receptivity of supersonic and hypersonic

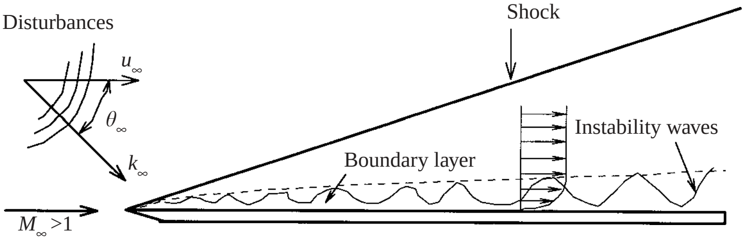

FIGURE 1. A diagram of the receptivity to free-stream disturbances for a supersonic boundary-layer flow over a flat plate.

boundary layers. Such simplification is acceptable in the linear stability analysis of supersonic boundary layers (Mack 1984) because the standoff distance of the shock from the wall is relatively large compared with the boundary-layer thickness. For the study of the supersonic boundary-layer receptivity to free-stream disturbances, however, such simplification is not appropriate because the effects of the oblique shock on the receptivity can be significant. The free-stream forcing waves must pass the oblique shock wave before they enter the boundary layer to excite the Mack modes there. The interaction of the shock with the forcing waves result in complex wave patterns behind the shock. Therefore, it is necessary to include the shock interaction in studies of supersonic boundary-layer receptivity mechanisms.

The DNS approach studies the boundary-layer receptivity process by numerically solving the time-dependent three-dimensional Navier–Stokes equations for the temporally or spatially evolving instability waves. Such a simulation requires that all relevant time and length scales in the flow field are resolved by the numerical solutions. Therefore, highly accurate high-order numerical methods are required for such direct simulations. One of the difficulties in supersonic flow simulations is that, owing to numerical instability, high-order linear schemes can only be used for the spatial discretization of the equations for the flow field without shock waves inside. Zhong (1998) presented and validated a new high-order (fifth- and sixth-order) upwind finite-difference shock-fitting method for the DNS of supersonic and hypersonic flows with a strong bow shock and with stiff source terms. The use of the shock-fitting method makes it possible to simulate unsteady motion of the shock accurately without spurious numerical noise. The method has been subsequently validated and applied to numerical studies of receptivity of two- and three-dimensional supersonic and hypersonic flows over blunt bodies, which has proved to be the most appropriate tool in such receptivity studies.

This paper is part 1 of a series of our extensive studies on the receptivity mechanisms of a supersonic boundary layer over a flat plate by DNS and by using the LST. The characteristics of boundary-layer normal modes are analysed in part 1. In part 2 (Ma & Zhong 2003), the receptivity mechanisms of a supersonic boundary layer to free-stream sound will be investigated.

2. Governing equations and physical model

Under a thermally and calorically perfect gas regime, the two-dimensional Navier–Stokes equations in conservative form can be written as:

$$\frac{\partial \boldsymbol{U}^*}{\partial t^*} + \frac{\partial}{\partial x^*}(\boldsymbol{F}_1^* + \boldsymbol{F}_{v1}^*) + \frac{\partial}{\partial y^*}(\boldsymbol{F}_2^* + \boldsymbol{F}_{v2}^*) = 0, \tag{1}$$

where the superscript '*' represents dimensional variables, and $\boldsymbol{U}^*$ is a vector containing the conservative variables, $\{\rho^*, \rho^* u^*, \rho^* v^*, e^*\}$. $\boldsymbol{F}_1^*$ and $\boldsymbol{F}_2^*$ are inviscid flux vectors, i.e.

$$\boldsymbol{F}_1^* = \begin{bmatrix} \rho^* u^* \\ \rho^* u^{*2} + p^* \\ \rho^* u^* v^* \\ u^*(e^* + p^*) \end{bmatrix}, \quad \boldsymbol{F}_2^* = \begin{bmatrix} \rho^* v^* \\ \rho^* u^* v^* \\ \rho^* v^{*2} + p^* \\ v^*(e^* + p^*) \end{bmatrix}. \tag{2}$$

$\boldsymbol{F}_{v1}^*$ and $\boldsymbol{F}_{v2}^*$ are viscous and diffusive flux vectors given by

$$\boldsymbol{F}_{v1}^* = \begin{bmatrix} 0 \\ -\tau_{xx}^* \\ -\tau_{xy}^* \\ -\tau_{xx}^* u^* - \tau_{xy}^* v^* - \kappa^* \frac{\partial T^*}{\partial x^*} \end{bmatrix}, \quad \boldsymbol{F}_{v2}^* = \begin{bmatrix} 0 \\ -\tau_{yx}^* \\ -\tau_{yy}^* \\ -\tau_{yx}^* u^* - \tau_{yy}^* v^* - \kappa \frac{\partial T^*}{\partial y^*} \end{bmatrix}, \tag{3}$$

where

$$p^* = \rho^* R^* T^*, \tag{4}$$

$$e^* = \rho^* c_v^* T^* + \tfrac{1}{2}\rho^*(u^{*2} + v^{*2}), \tag{5}$$

$$\tau_{ij}^* = \mu^* \left(\frac{\partial u_i^*}{\partial x_j^*} + \frac{\partial u_j^*}{\partial x_i^*} \right) - \tfrac{2}{3}\mu^* \tfrac{\partial u_k^*}{\partial x_k^*} \delta_{ij}, \tag{6}$$

for $i, j = 1, 2$, $(u_1^*, u_2^*) = (u^*, v^*)$. μ^* is the viscosity coefficient and calculated by using Sutherland's law:

$$\mu^* = \mu_r^* \left(\frac{T^*}{T_r^*} \right)^{3/2} \frac{T_r^* + T_s^*}{T^* + T_s^*}, \tag{7}$$

and κ^* is the heat conductivity coefficient computed by assuming a constant Prandtl number $Pr = 0.72$, where the Prandtl number is defined as $Pr = \mu^* c_p^* / \kappa^*$.

In this paper, dimensional flow variables are non-dimensionalized by the steady-state free-stream conditions. Specifically, velocities are non-dimensionalized by the free-stream velocity u_∞^*, length scales by a boundary-layer thickness length L^* given by (9), density by ρ_∞^*, pressure by p_∞^*, temperature by T_∞^*, time by L^*/u_∞^*, vorticity by u_∞^*/L^*, entropy by c_p^*, wavenumber by $1/L^*$, circular frequency by u_∞^*/L^*, etc. The dimensionless flow variables are denoted by the same notation as their dimensional counterparts, but without the superscript.

3. Numerical methods and boundary conditions

A fifth-order shock-fitting method of Zhong (1998) is used to compute the two-dimensional Navier–Stokes equations in the flow field bounded by the bow shock and the plate (figure 1). The numerical method is described briefly here.

The shock-fitting method treats the bow shock as a computational boundary. The flow variables behind the shock are determined by the Rankine–Hugoniot relations across the shock and a characteristic compatibility equation from behind the shock. The Rankine–Hugoniot relations lead to jump conditions for flow variables behind the moving shock as functions of unsteady free-stream flow variables in front of the shock and the local shock normal velocity v_n. In order to compute the flow variables behind the shock, the velocity of the shock front v_n is required, which is determined by a characteristic compatibility equation immediately behind the shock. The transient movement of the shock and its interaction with free-stream disturbance waves are solved as a part of the solutions. The use of the shock-fitting method makes it possible to use high-order finite-difference schemes for spatial discretization. A fifth-order upwind finite-difference scheme is applied for convective terms while a sixth-order central scheme is used for the discretization of viscous terms. The spatial discretization of governing equations leads to a system of first-order ordinary differential equations. The first-order explicit Runge–Kutta method is used for temporal discretization. The computer code based on the fifth-order shock-fitting method has been tested in the study of receptivity of blunt body to free-stream disturbances (Zhong 2001). This code is applied to the current study of the receptivity to free-stream disturbances of supersonic flow over a flat plate.

As a part of the shock-fitting method, Rankine–Hugoniot relations are used to determine steady or unsteady flow variables at locations immediately behind the shock boundary. High-order extrapolation is used for outflow conditions because the flow is supersonic at the outlet except that there is a tiny region near the wall where flow is subsonic. The non-slip wall-boundary condition is used for velocity. The adiabatic wall-boundary condition is used for the steady base flow. For unsteady flow simulations, the conditions for temperature fluctuations at the wall are either $\partial T'/\partial y = 0$ or $T' = 0$. Although adiabatic wall and isothermal wall boundary conditions are commonly used for the base steady flow, $\partial T'/\partial y|_{y=0} = 0$ is called the adiabatic wall and $T'|_{y=0} = 0$ is called the isothermal wall in this paper to avoid confusion. It has been argued (Mack 1984; Malik 1990) that it is more physical to assume that the temperature perturbations vanish at the solid boundary even though the adiabatic wall-boundary condition can be used in base flow calculation. The main argument for this assumption is that for high-frequency disturbances, the temperature fluctuations will not penetrate deep into the solid boundary owing to the thermal inertia of the solid body. In reality, the temperature perturbations could be somewhere between zero perturbation and zero normal gradient for adiabatic conditions. Therefore, in this paper, both the adiabatic wall and isothermal wall boundary conditions are used for the temperature perturbations as two bounds for real cases if the physical condition for temperature perturbations is difficult to determine. The effect of both wall temperature boundary conditions on the growth rates of boundary-layer instability waves will be investigated and discussed.

For supersonic flow over a flat plate with a sharp leading edge, there exists a singular point at the tip of the leading edge, which introduces numerical instability in a simulation using the fifth-order shock-fitting method. Therefore, the computational domain for a shock-fitting calculation starts from a very short distance downstream of the leading edge. A set of inflow conditions at this inlet location are required to initialize the flow simulation by the shock-fitting method. In fact, setting physical inflow conditions correctly is important for both temporal and spatial DNS for supersonic and hypersonic flow over a flat plate. To our knowledge, all previous DNS works on supersonic flow over flat plates use locally self-similar solutions of boundary-layer equations under the assumption $\partial p/\partial x = 0$ as inflow conditions and shock waves are excluded from consideration. However, the zero-pressure-gradient boundary-layer solutions are not valid for solutions near the leading edge owing to the interaction between the boundary layer and the outer supersonic flow. Such interaction leads to a favourable pressure gradient and the formation of an oblique shock in the flow field. Such effects must be accurately accounted for in the numerical simulations by using a high-order shock-fitting scheme. In this paper, the steady-state inflow conditions near the leading edge for the shock-fitting calculations are obtained from the results computed by the second-order total variation diminishing (TVD) shock-capturing scheme in a very small region including the leading edge. The results of code validation and the evaluation of numerical accuracy for the solutions have been presented in Ma & Zhong (2001).

4. Flow conditions of Mach 4.5 flow over a flat plate

The receptivity of a Mach 4.5 boundary-layer flow over a flat plate is considered because the stability of Mach 4.5 flow has been extensively studied (Kendall 1967; Bayliss, Maestrello & Krishnan 1991; Kerschen 1989; Pruett & Chang 1993; Kleiser, Guo & Adams 1996). The flow conditions are the same as those used in Kendall's (1975) experiment on the stability of a Mach 4.5 flow over a flat plate, i.e.

$$M_\infty = 4.5, \qquad T^*_\infty = 65.15\,\mathrm{K},$$

$$p^*_\infty = 728.4381557\,\mathrm{Pa}, \qquad Pr = 0.72,$$

$$\text{Unit Reynolds number: } Re^*_\infty = \frac{\rho^*_\infty u^*_\infty}{\mu^*_\infty} = 7.2 \times 10^6\ \mathrm{m}^{-1}.$$

In many figures in this paper, the results are plotted as a function of the dimensional x^* coordinate along the flat plate because this case has been studied by previous experiments. The dimensional x^* coordinate in the figures can be converted easily to dimensionless local Reynolds numbers according to the following formula:

$$Re_x = Re^*_\infty\, x^* = 7.2 \times 10^6 x^*, \tag{8}$$

where x^* is the dimensional coordinate in metres measured from the leading edge along the plate surface for the current case.

In this paper, a TVD code developed by Zhong & Lee (1996) is used to compute steady supersonic flow over the leading edge of a flat plate. The TVD code has been validated by comparing numerical results with experimental results in several cases (Ma & Zhong 2001). The steady flow near the leading edge of an infinitely thin flat plate is calculated on very fine grids (200×200, $\Delta x^* = 5 \times 10^{-5}\,\mathrm{m}$) by using the same TVD code. The TVD solutions of the flow in the leading-edge region are then used as inflow conditions to start the simulation by the fifth-order shock-fitting method. Figure 2(*a*) compares the steady pressure contours obtained from the TVD method with those from the fifth-order shock-fitting method. Overall, there is excellent agreement between the solutions of the two methods for steady flow. There exists some minor visible difference in the downstream area between the contours from the two different methods owing to the low-order accuracy and high dissipation associated with the TVD method. However, it is accurate enough to use TVD solutions as inflow conditions for the subsequent high-order shock-fitting calculations. Figure 2(*b*) compares the profiles of normal velocity at $x^* = 0.007\,\mathrm{m}$ for solutions computed by the two methods. The agreement between the two sets of results computed by the TVD scheme and by the high-order shock-fitting scheme is excellent. Therefore, the TVD solutions are used as the steady inflow conditions to start our high-order calculation by using the shock-fitting method.

The computational domain of the current simulations by using the shock-fitting method begins at $x^* = 0.006\,\mathrm{m}$ and ends at $0.63\,\mathrm{m}$, corresponding to the local Reynolds

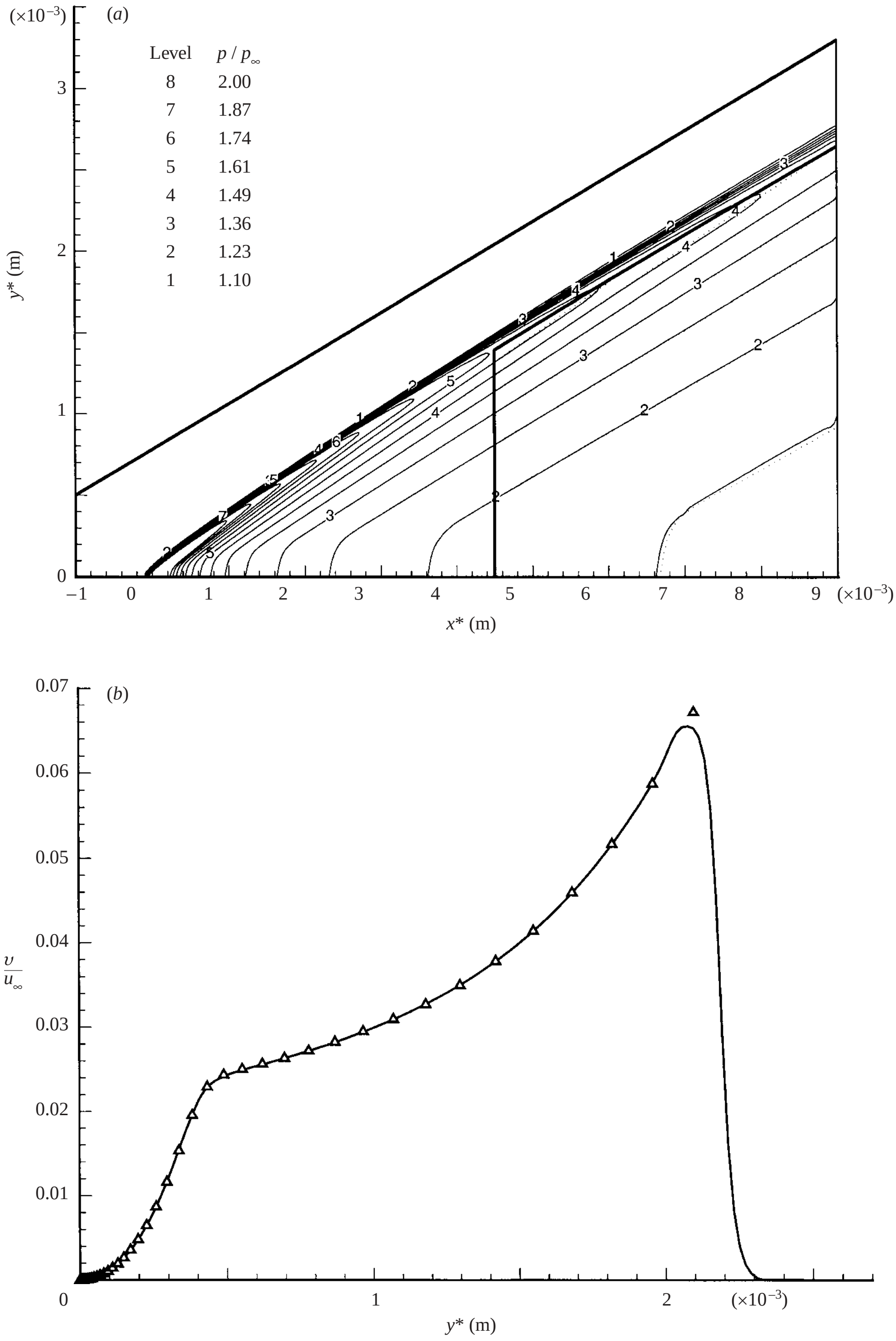

FIGURE 2. (*a*) Steady pressure contours in a local region near the leading edge and (*b*) the profiles of steady normal velocity components along a wall-normal grid line located at $Re_x = 50\,400$. The vertical line in the middle of the domain is the inlet for the shock-fitting calculation. ($Re_x = 7.2 \times 10^6 x^*$ and $M_\infty = 4.5$). (*a*) —, TVD; …, SHKFIT. (*b*) —, TVD; Δ, SHKFIT.

numbers ranging from $Re_x = 4.32 \times 10^4$ to $Re_x = 4.54 \times 10^6$. In studies of boundary-layer stability, a local Reynolds number, R, based on the length scale of the boundary-layer thickness are often used:

$$R = \sqrt{Re_x} = \frac{\rho_\infty^* u_\infty^* L^*}{\mu_\infty^*}, \quad L^* = \sqrt{\frac{\mu_\infty^* x^*}{\rho_\infty^* u_\infty^*}}, \tag{9}$$

where L^* is the length scale of the boundary-layer thickness. In terms of R, the full computational domain of current simulations spans from $R = 207.9$ to $R = 2129.8$. In actual simulations, the computational domain is divided into 11 subzones, a total of 3121 grid points in the streamwise direction and 121 grid points in the wall-normal direction. In the streamwise direction, there are about 17 grid points to resolve one wavelength of the second mode at $F = 2.2 \times 10^{-4}$. From supersonic boundary-layer self-similarity solutions, the displacement thickness of the current boundary layer is approximately $12.9L^*$. A grid stretching function is used in the wall-normal direction to cluster more points inside the boundary layer near the wall. The grid points are distributed uniformly in the streamwise direction. In temporal integration, the time step is calculated by fixed CFL number 0.05.

For unsteady calculation, the frequency is often characterized by a dimensionless frequency F defined as

$$F = \frac{\omega^* \mu_\infty^*}{\rho_\infty^* u_\infty^{*2}}, \tag{10}$$

where ω^* is dimensional circular frequency. In this paper, boundary-layer normal modes with four different frequencies, $F = 0.6 \times 10^{-4}$, 1.2×10^{-4}, 1.6×10^{-4} and 2.2×10^{-4}, are considered.

5. Steady base flow solutions

The steady-flow solutions are first obtained by using the shock-fitting scheme for the Mach 4.5 flow over a flat plate without any free-stream disturbances. Figure 3 shows the distribution of pressure along the wall surface. There are significant pressure gradients in the streamwise direction, especially in the region near the leading edge, resulting from the interaction between inviscid external flow and viscous boundary-layer flow.

Figure 4 shows the positions and angles of the oblique shock wave induced by the boundary-layer displacement effect. The shock wave is almost a straight line and shock angles decrease from 15.8° near the leading edge to 13.4° at the exit of the current computational domain. There is significant change in shock angles near the leading edge owing to the interaction between the shock wave and the boundary layer. In the downstream region, the shock moves far away from the boundary layer and the interaction between the inviscid flow and the boundary layer becomes negligible. As a result, local shock angles in the downstream region approach the limit of Mach angle at 12.84° for the Mach 4.5 flow.

It is well known that the second wall-normal derivative of u is critical to the stability of the second mode. The comparison of profiles of the second wall-normal derivative of u ($x = 0.139$m, $R = 1000$) between the shock-fitting method and the boundary-layer approach is presented in figure 5. There is good agreement between the boundary-layer self-similar solution and the simulation except for a visible difference located near

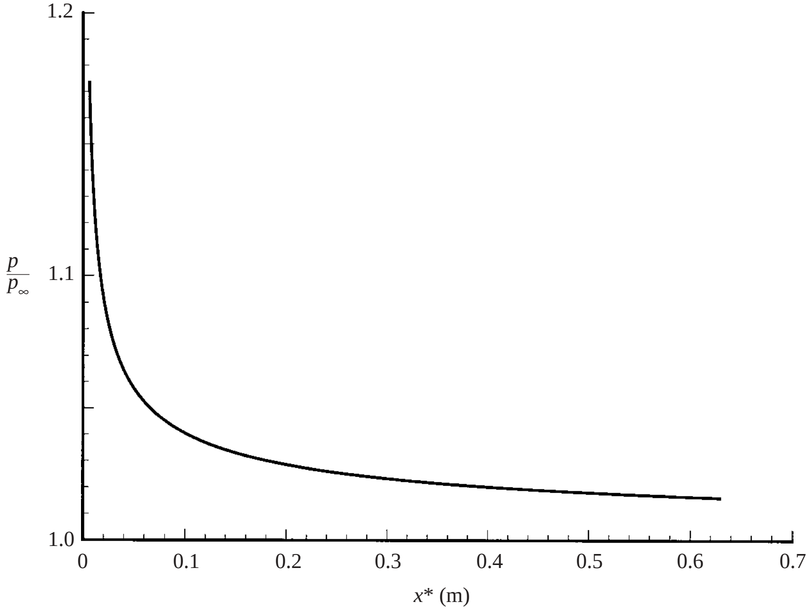

FIGURE 3. Pressure distribution along the plate surface for steady base flow solutions obtained by using the fifth-order shock-fitting method.

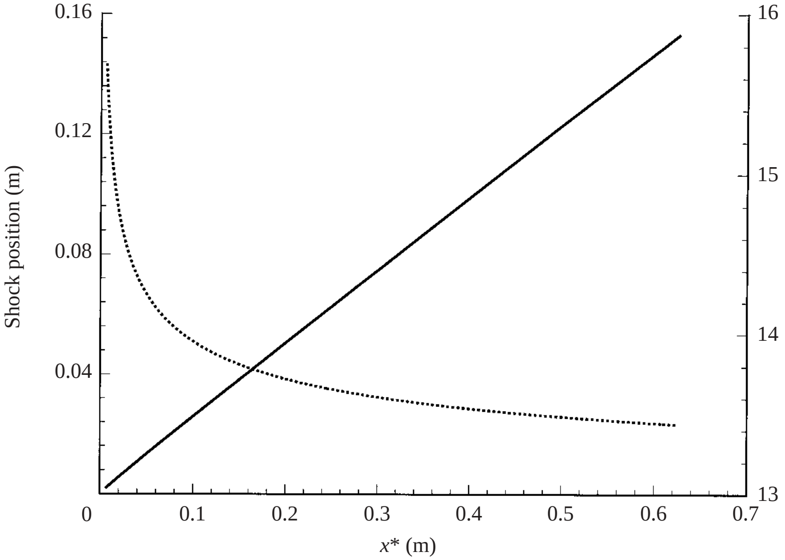

FIGURE 4. —, Position and . . . , angle of oblique shock wave in steady base flow.

the edge of the boundary layer ($\delta^* = 12.9L^*$), because pressure gradients are ignored in the boundary-layer approach. Other features of the steady solutions for this flow are not presented here because they are similar to the boundary-layer self-similar solutions.

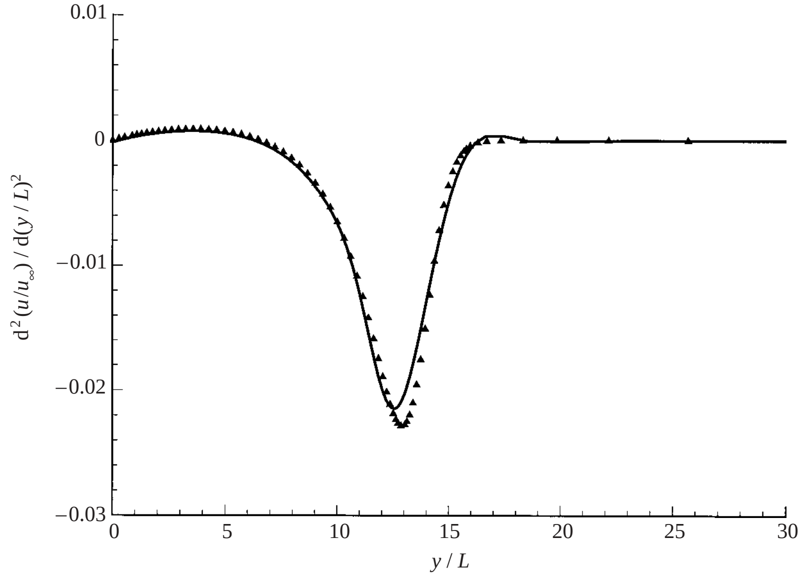

FIGURE 5. Comparison of profiles of second wall-normal derivative of u ($x^* = 0.139$ m, $R = 1000$). —, SHKFIT; ▲, BL.

6. Boundary-layer wave mode characteristics

The instability waves in supersonic boundary layers, such as the first and the second modes, have been studied extensively by Mack (1984) and other workers by using the LST approach. These previous LST studies have been mainly focused on the instability of the first- and second-mode waves. However, in a receptivity process, it is found that some other wave modes, which are stable in a linear stability analysis, play an important role in the receptivity process. The stable wave modes generated by the forcing waves can interact with the instability waves once they are generated. In order to understand the receptivity process, it is necessary to understand the characteristics of these stable wave modes. Therefore, as the first step in studying the receptivity of a supersonic boundary layer to free-stream disturbances, the characteristics of normal modes of the Mach 4.5 boundary layer are studied by the LST in this section.

In the LST studies, pressure is usually non-dimensionalized by $\rho_\infty^* u_\infty^{*2}$, and circular frequency ω^* is normalized by u_∞^*/L^*. The relation between non-dimensional circular frequency ω and F is

$$\omega = RF. \tag{11}$$

The LST is based on the normal mode analysis under a parallel-flow assumption. The formulation of the LST was described in detail in Malik (1990). An LST computer code based on the multi-domain spectral method of Malik (1990) is developed and validated.

6.1. *Modes I, II, III and IV*

After the validation of the LST code, the characteristics of Mach 4.5 ($Re_\infty^* = 7.2 \times 10^6\ \mathrm{m}^{-1}$) boundary-layer normal modes are studied by using the same LST code. As shown in figure 5, there is little difference between self-similar boundary-layer solutions and steady-flow solutions from numerical simulations. Our calculations have shown that the linear stability properties based on steady flow solutions from

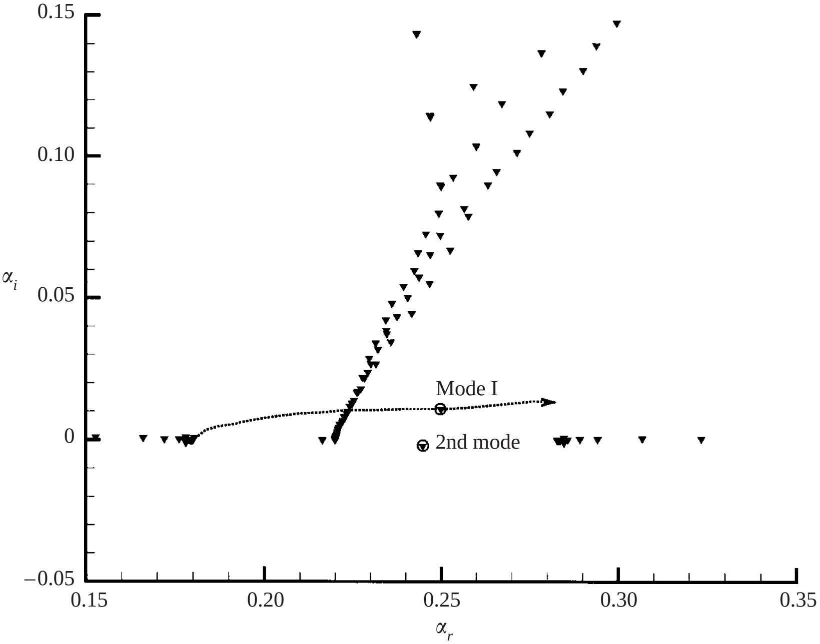

FIGURE 6. Spectra of eigenvalues with $F = 2.2 \times 10^{-4}$ and $R = 1000$.

numerical simulations are very close to those based on self-similar boundary-layer solutions. The base flows obtained from self-similar boundary-layer solutions are used to perform the LST because it is much easier to obtain self-similar base flow solutions at arbitrary locations.

In the first test case, the eigenvalues α associated with two-dimensional disturbance modes are identified with fixed frequency $F = 2.2 \times 10^{-4}$ and spanwise wavenumber $\beta = 0$. Here, the adiabatic boundary condition for temperature disturbances is used. Figure 6 shows the spectra of eigenvalues at station $R = 1000$ ($x^* = 0.139$). Here, there are two discrete modes highlighted by circles in the spectra. One is the well-known second mode; the other is called mode I in this paper. When the test station gradually moves from upstream to downstream and R increases little by little, the relative positions of mode I and the second mode will gradually change. We can track the position of each mode and obtain their trajectories. The dashed line in figure 6 represents the trajectory and direction of mode I when R changes from low to high. It shows that mode I starts from the continuous spectra on the left of the spectra, and passes across another continuous spectra in the middle with increasing R. Here, it is necessary to describe in detail how to track a mode by the LST when it passes across continuous spectra. In fact, there are two multi-domain spectral methods (Malik 1990) to carry out the LST. One is the global method and the other is the local method. The global method can be used to generate the complete spectra of all eigenvalues. The local method is a shooting method, which can obtain a more accurate eigenvalue of a specific normal mode, when the less accurate eigenvalue from the global method is used as an initial guess. We can also use the eigenvalue of a normal mode at the current station as the initial guess to shoot the eigenvalue of the same mode for the next neighbouring station. Once we identify the eigenvalue of a normal mode at the current station, we can track this mode upstream or downstream from the current station to

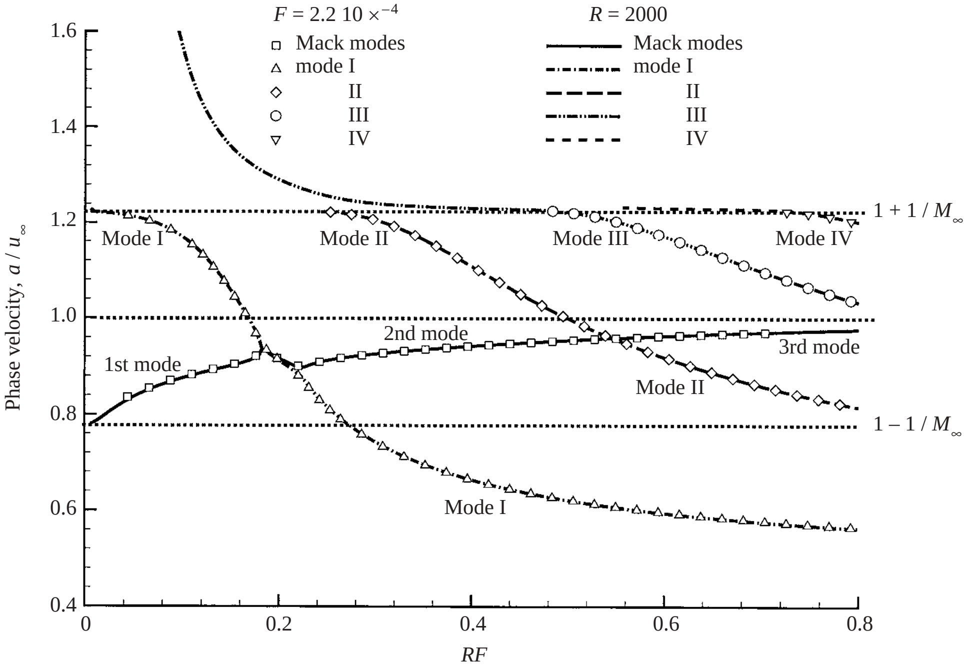

FIGURE 7. The distribution of the phase velocities of boundary-layer wave modes as a function of RF obtained by the LST, either at different R with a fixed $F = 2.2 \times 10^{-4}$ or at different F with a fixed location at $R = 2000$ ($M_\infty = 4.5$ and $Re^*_\infty = 7.2 \times 10^6\ \mathrm{m}^{-1}$).

obtain the trajectory of this mode. By the local method, we can track the interested mode in the crossing regions. In the same way, we can find the trajectories of mode I, the second mode and other modes. After the complex parameter α is found, a non-dimensional phase velocity of the normal mode can be calculated as

$$a = \frac{\omega}{\alpha_r}. \tag{12}$$

Either the phase velocity a or the real part of the wavenumber α_r can be used to characterize the normal mode inside the boundary layer.

Figure 7 shows the distributions of the phase velocities of boundary-layer wave modes. The phase velocity distributions shown in this figure include the following two computational cases:

> Case 1: phase velocity distributions as a function of different streamwise locations R at a fixed frequency of $F = 2.2 \times 10^{-4}$.
>
> Case 2: phase velocity distributions as a function of different frequencies F at a fixed streamwise location of $R = 2000$.

The figure shows that the two cases have identical phase velocity curves when they are plotted as functions of $\omega = RF$. In general, the phase velocities (or α_r) of different normal modes inside the boundary layer can be written as a function of non-dimensional circular frequency ω for cases of different frequencies F and different local Reynolds numbers R.

Figure 7 presents the phase velocities of the first several wave modes in the supersonic boundary layer. The phase velocities of the fast acoustic wave $(1 + 1/M_\infty)$,

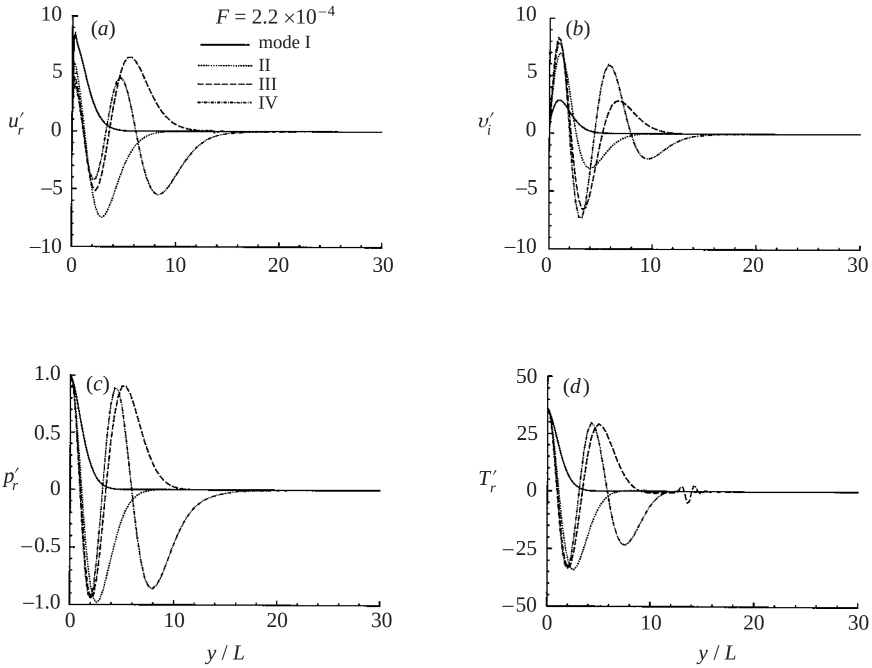

FIGURE 8. Profiles of stable boundary-layer normal modes (mode I, mode II, etc.) obtained by the LST ($M_\infty = 4.5$ and $R = 4000$).

entropy/vorticity wave (1), and slow acoustic wave ($1 - 1/M_\infty$) are also shown in the figure for comparison. In the figure, there is a class of wave modes, which originate with an initial phase velocity of the fast acoustic wave ($1 + 1/M_\infty$). Before these wave modes become distinct modes, their eigenvalues merge with the continuous spectra. After these wave modes appear, their phase velocities decrease gradually as they propagate downstream. In this paper, we define these wave modes as mode I, mode II, mode III, etc, according to the sequences of their appearance. Specifically, mode I appears from the leading edge; mode II comes out next, followed by mode III, and so on. At locations further downstream, even higher modes will appear. The trajectory of mode I in the spectra of eigenvalues is shown in figure 6. Here, mode I, mode II, and so on, are in fact ‘multiple-viscous solutions’ in Mack (1984) and in Eissler & Bestek (1996). We give them different names for convenience of discussion about receptivity studies.

Figure 8 shows the typical eigenfunction profiles of this class of modes at $R = 4000$ and $F = 2.2 \times 10^{-4}$. In this paper, profiles of all disturbances are normalized by non-dimensional pressure perturbation on the wall. At this location, there is only one peak for mode I disturbances, while there is one peak and one valley for mode II, two peaks and one valley for mode III , two peaks and two valleys for mode IV disturbances. This figure also shows that the disturbances of this family of modes are mainly concentrated inside the boundary layer (the boundary-layer displacement thickness is about $\delta^* = 12.9L^*$). When this class of disturbances propagates from upstream to downstream, the total number of peaks and valleys for pressure disturbance profiles does not change, although the locations of peaks and valleys can change gradually.

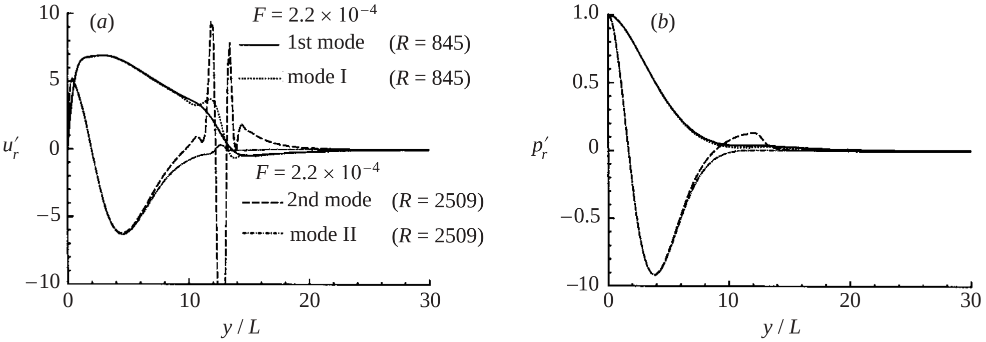

FIGURE 9. Comparison of profiles of modes I and II with the Mack modes (first and second modes) at the locations of the wave synchronization points.

6.2. *Mack modes* (*first, second and third modes*)

In addition to the family of wave modes I, II and III defined above, figure 7 shows that there is another wave mode starting from the leading edge with an initial phase velocity close to $1 - 1/M_\infty$ near the leading edge. For this mode, the phase velocity is less than the free-stream velocity, and approaches the value of the free-stream velocity as it propagates downstream. As shown in figure 7, the phase velocity curve of this mode intersects with modes I, II, III and IV subsequently as RF increases. It should be pointed out that this mode is in fact the first mode before it intersects with mode I. It becomes the second mode between mode I and mode II. After intersection with mode II, it becomes the third mode. It is well known that the first mode is a Tollmien–Schlichting mode in supersonic flow, which was demonstrated to be most unstable in some oblique angles (Dunn & Lin 1955). The second, third and higher modes are acoustic instability modes in supersonic and hypersonic boundary layers found by Mack (1984). As shown in figure 7, the first, second, third modes are in fact different sections of a single mode. Here, this mode is simply called Mack modes for convenience of discussion, because all the different parts of this mode are Mack modes except that the first part is the first mode.

At the intersections of the phase velocity curves in figure 7, the Mack modes are synchronized with mode I, mode II, mode III, or higher modes because they have the same frequency and phase velocity there. The synchronization of two different wave modes can lead to resonant interactions between them. Here, the ‘resonant interaction’ designates the interaction between different waves with close phase velocities and the same frequencies. Unlike modes I, II and III, whose numbers of peaks and valleys do not change as R increases for a fixed F, the total number of peaks and valleys for pressure disturbance profiles of the Mack modes increases gradually when the Mack mode waves propagate downstream. For example, near the leading edge, there is only one peak for the pressure disturbance profile of the Mack mode. After the synchronization with mode I, another valley appears in the pressure disturbance profile. Mack defined the numbering of these modes as the first mode with one peak in the pressure profile, the second mode with one peak and one valley, etc.

At the location of synchronization between the first mode and mode I ($R = 845$ for $F = 2.2 \times 10^{-4}$), both the first mode and mode I have almost the same profiles of disturbances inside the boundary layer (figure 9). As a result, it is almost impossible to distinguish mode I from the first mode based on the profiles of disturbances at this location. Because both the first mode and mode I have the same phase velocity at their synchronization location, it is impossible to identify them from the phase velocity either. The characteristic that can distinguish them is the change of phase velocities during propagation. The phase velocity of mode I decreases while that of the first mode increases during their propagation downstream. After the synchronization point between mode I and the first mode, another valley gradually appears in the profile of pressure disturbances for the Mack mode. The Mack mode in this region is called the second mode. When the second mode propagates further downstream, it becomes synchronized with mode II. At the location of synchronization ($R = 2509$ for $F = 2.2 \times 10^{-4}$), both the second mode and mode II have almost the same profiles of disturbances inside the boundary layer (figure 9). Figure 9 also shows that there is much stronger oscillation in the profiles of the second mode disturbances near the edge of the boundary layer ($\delta^* = 12.9L^*$) compared with that of mode II. At the location of Mack-mode synchronization with mode II, another peak appears in the profile of pressure disturbances for the Mack mode, which is the characteristic of the third mode based on Mack's definition. Actually, the profiles of the Mack mode at $R = 2509$ shown in figure 9 are located in the transition region from the second mode to the third mode. Similarly, the Mack mode will become synchronized with mode III and become the fourth mode when it propagates further downstream (figure 7).

6.3. *Effects of Reynolds numbers and frequencies*

Figure 7 shows that the effects of changing Reynolds number R and frequency F on the wave modes can be represented by a combined parameter RF. This figure shows two groups of computational cases: (i) different F at fixed $R = 2000$, and (ii) different R at fixed $F = 2.2 \times 10^{-4}$. The adiabatic boundary condition for the temperature disturbances is used for both groups. In figure 7, different lines show the phase velocities of different normal modes changing with ω ($\omega = RF$). It shows that the phase veloicty curves of a given mode are the same when the phase velocities are plotted against ω, for the two groups of cases. Therefore, the phase velocities of normal modes are functions of the product of non-dimensional frequency and Reynolds number (RF). Figure 7 also shows that $1 + 1/M_\infty$ is not the limit for the phase velocities of modes I, II, III, etc. However, these modes merge with continuous spectra when their phase velocities are greater than $1 + 1/M_\infty$.

6.4. *Stability of boundary-layer normal modes*

The phase velocity distributions of disturbances combined with growth rates (α_i) and disturbance profiles are important parameters to identify different normal modes. The growth rates of different normal modes for the previous two groups of computational cases are plotted in figure 10. In this figure, different symbols stand for the first group of cases of different R at a fixed frequency of $F = 2.2 \times 10^{-4}$, and line patterns represent the second group of cases of different F at a fixed Reynolds number of $R = 2000$. For both groups of cases, the growth rates for modes I, II, III and IV are always positive, which means this family of modes are always stable. Furthermore, the values of α_i of these modes increase as they propagate downstream, which indicates that these modes become more and more stable during their propagation downstream. Figure 10 also shows that the Mack modes are unstable in the range of RF between 0.18 and 0.23, in which the unstable Mack modes are the conventional second mode. In this range, the growth rates of the second mode change dramatically. As shown in the figure, the slope of the growth rate curve for the second mode is very sharp

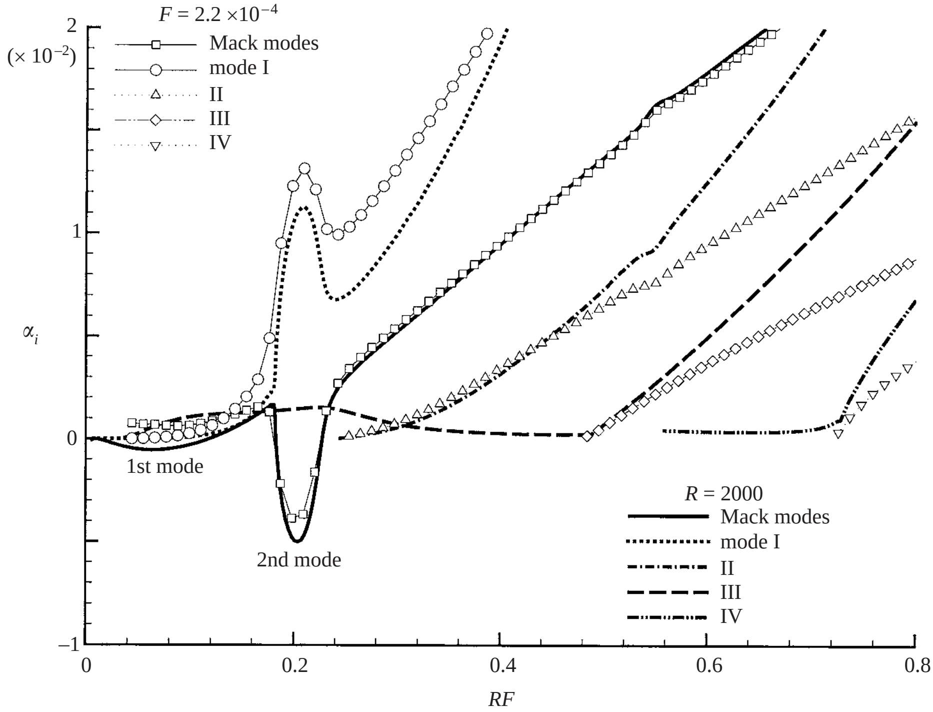

FIGURE 10. The distribution of the growth rates of boundary-layer wave modes as a function of RF obtained by the LST.

in this range. The shape of growth rate curve of the unstable second mode is almost the same for the two groups of cases of fixed frequency at $F = 2.2 \times 10^{-4}$ and fixed Reynolds number at $R = 2000$. In addition, the locations of branch I and II neutral stability points of the second mode in terms of RF are almost same for both group of computational cases.

Figure 10 also shows the conjugation between the second mode and mode I. In the second-mode unstable region, when the growth rates of the second mode decrease, the growth rates of mode I increase, and vice versa. The second Mack mode becomes more unstable while mode I becomes more stable after they are synchronized with each other. At the valley of the growth rate curve for the second mode, the growth rates of mode I reach the local peak value. In the range from $RF = 0.006$ to $RF = 0.118$, the Mack mode is unstable for the fixed Reynolds number $R = 2000$ case, although the results of the fixed frequency $F = 2.2 \times 10^{-4}$ case show that the Mack mode is stable in the same range. The Mack mode in this range is the conventional first mode. According to Mack's study, the oblique first mode ($\beta > 0$) is most unstable, while the second mode is most unstable when $\beta = 0$. The growth rates of the Mack modes at different wave angle $\psi = \arctan(\beta/\alpha_r)$ are shown in figure 11(a). It is obvious that the results are consistent with Mack's results, i.e. the oblique first mode is most unstable when ψ is about 60° and the two-dimensional second mode is most unstable. In the case of fixed $F = 2.2 \times 10^{-4}$, the first mode gradually becomes unstable with increases of wave angle ψ, although it is stable for two-dimensional disturbances ($\psi = 0$). In addition, the most unstable wave angles are different for cases of different locations R. When ψ is larger than 45°, the second mode becomes always stable. Figure 11(a)

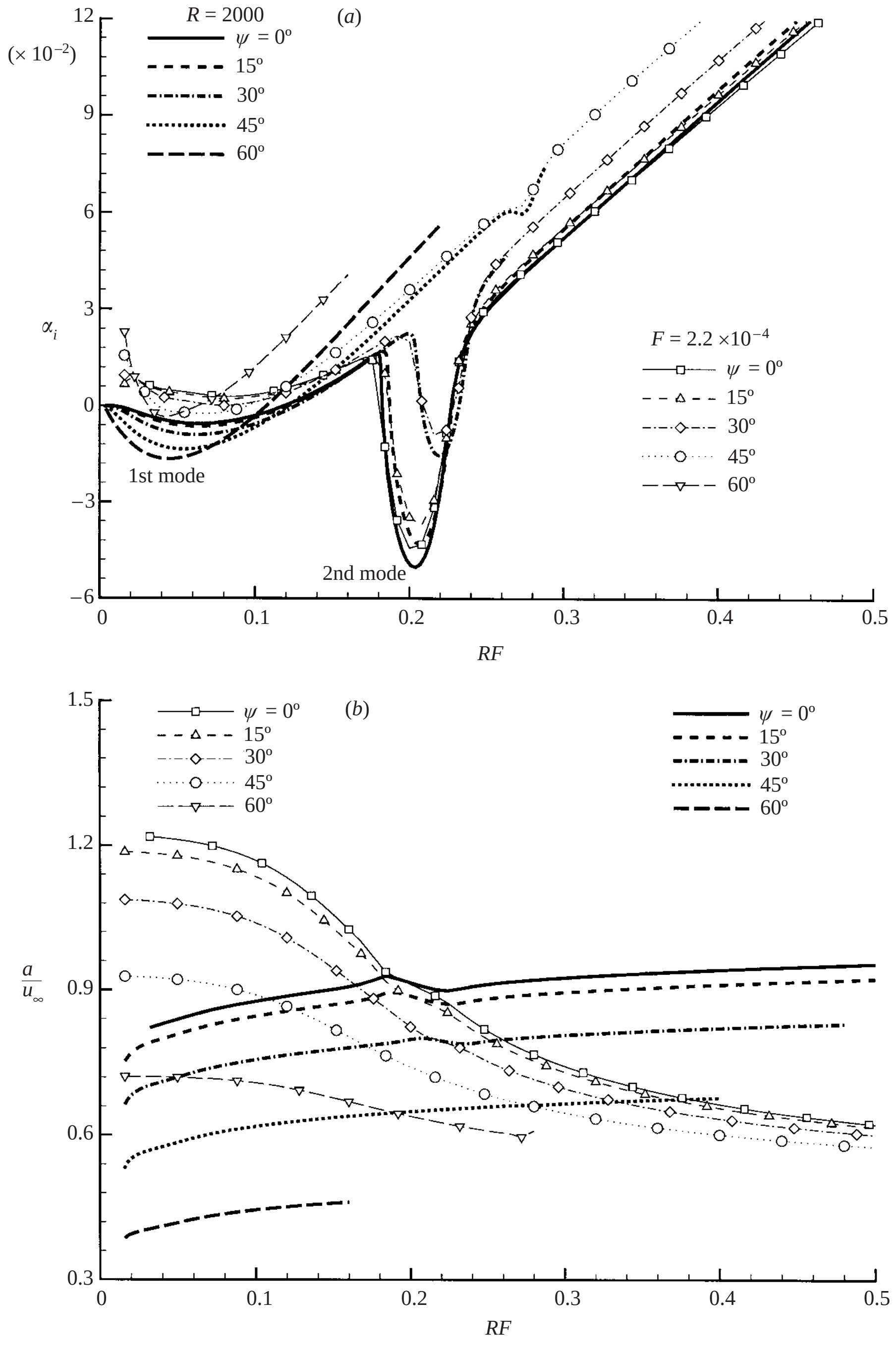

FIGURE 11. The distribution of the growth rates of (*a*) Mack modes and (*b*) the phase velocities of three-dimensional boundary-layer wave modes at different wave angles as a function of *RF* obtained by the LST.

also shows that the growth rate curves at different wave angles ψ are very similar for the fixed $F = 2.2 \times 10^{-4}$ case and the fixed $R = 2000$ case. Almost the same locations of branch I or II neutral stability points of the second mode in terms of *RF* are obtained for different angles in both groups of cases. Modes I, II, III and IV are always stable at any wave angles. The phase velocity curves at different wave angles ψ are shown in figure 11(*b*). It is obvious that the phase velocities are smaller at larger wave angles at the same location. Again, the same structures of phase velocity curves *vs.* RF at different wave angles are obtained for both groups of cases.

Fedorov & Khokhlov (2002, figure 1) obtained very similar structures of phase velocity and stability curves of mode I and Mack modes. Though direct comparison with Fedorov & Khokhlov's results is not possible because of different flow conditions, the general trend of phase velocity and stability curves of boundary-layer normal modes of current results is consistent with that of Fedorov & Khokhlov's theoretical analysis. It should be noted that mode I was called the first mode in Fedorov & Khokhlov (2002). According to the stability properties of different modes, the oblique first mode ($\beta > 0$) is most unstable, while the second mode is two-dimensional dominant. The first, second and third modes are in fact different sections of a single Mack mode, as shown in figure 7.

6.5. *Effect of temperature boundary condition at the wall*

To study the effect of the wall boundary condition for temperature perturbations on the stability characteristics of the boundary-layer normal modes, eigenvalues associated with different modes at fixed location ($R = 2000$) are obtained for a range of frequencies with both isothermal and adiabatic wall boundary conditions. The results of the isothermal case are compared with those of the adiabatic case. Figure 12 compares the phase velocities and the growth rates of the relevant normal modes as a function of ω ($\omega = RF$). Different line patterns show the phase velocities of different normal modes for the isothermal case while different symbols denote those for the adiabatic case. The figure shows that the phase velocities of normal modes are the same for both the isothermal case and the adiabatic case, which shows that the effect of the wall temperature disturbance boundary condition on the phase velocities is very small. This figure also shows that all normal modes of the isothermal case are more stable than the corresponding modes of the adiabatic case. This is consistent with Eissler & Bestek's (1995) simulation results. It showed in Eissler & Bestek's (1995) study on wall-temperature effects on transition in supersonic boundary layers that adiabatic disturbances led to a significantly lower transition Reynolds number than the non-fluctuating temperature condition.

6.6. *Exchange between different normal modes*

In this test case, a lower fixed frequency of $F = 0.6 \times 10^{-4}$ is used in the LST analysis. We chose a lower frequency because the mode exchange between different normal modes is clearly shown at the frequency $F = 0.6 \times 10^{-4}$, whereas this phenomenon does not present at frequency $F = 2.2 \times 10^{-4}$ in the LST results. The eigenvalues associated with different modes are identified and tracked from upstream to downstream with fixed spanwise wavenumber $\beta = 0$. An adiabatic boundary condition for the temperature disturbances is used. Figure 13(*a*) compares the phase velocities of different normal modes changing with the Reynolds numbers for the current case with those from the previous case of higher frequency at $F = 2.2 \times 10^{-4}$. The phase velocity curves for the $F = 0.6 \times 10^{-4}$ case match well with those of the $F = 2.2 \times 10^{-4}$ case. However, different from the case of $F = 2.2 \times 10^{-4}$, figure 13(*a*) shows a wave mode exchange between mode I and the Mack mode for the case of $F = 0.6 \times 10^{-4}$. After the first mode becomes synchronized with mode I, the first mode changes to

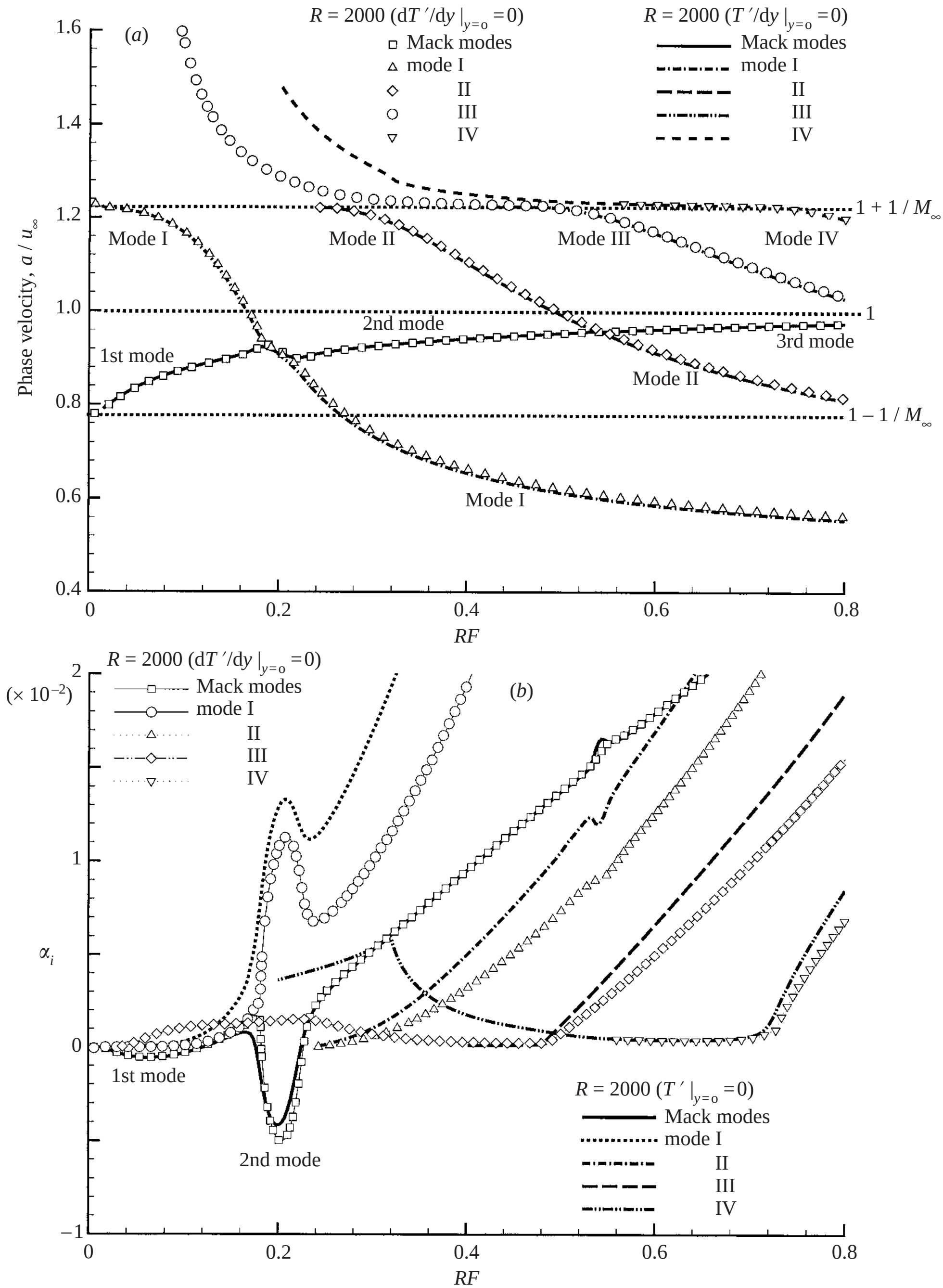

FIGURE 12. Comparison of (*a*) phase velocities and (*b*) growth rates of boundary-layer normal modes between the isothermal case and the adiabatic case.

mode I while mode I changes to the second mode for the current case. Such mode exchange was first found by Fedorov & Khokhlov (2001). At the synchronization point between mode I and the first mode ($R = 3100$ for $F = 0.6 \times 10^{-4}$ and $R = 845$ for $F = 2.2 \times 10^{-4}$), the first mode and mode I have very similar disturbance structures

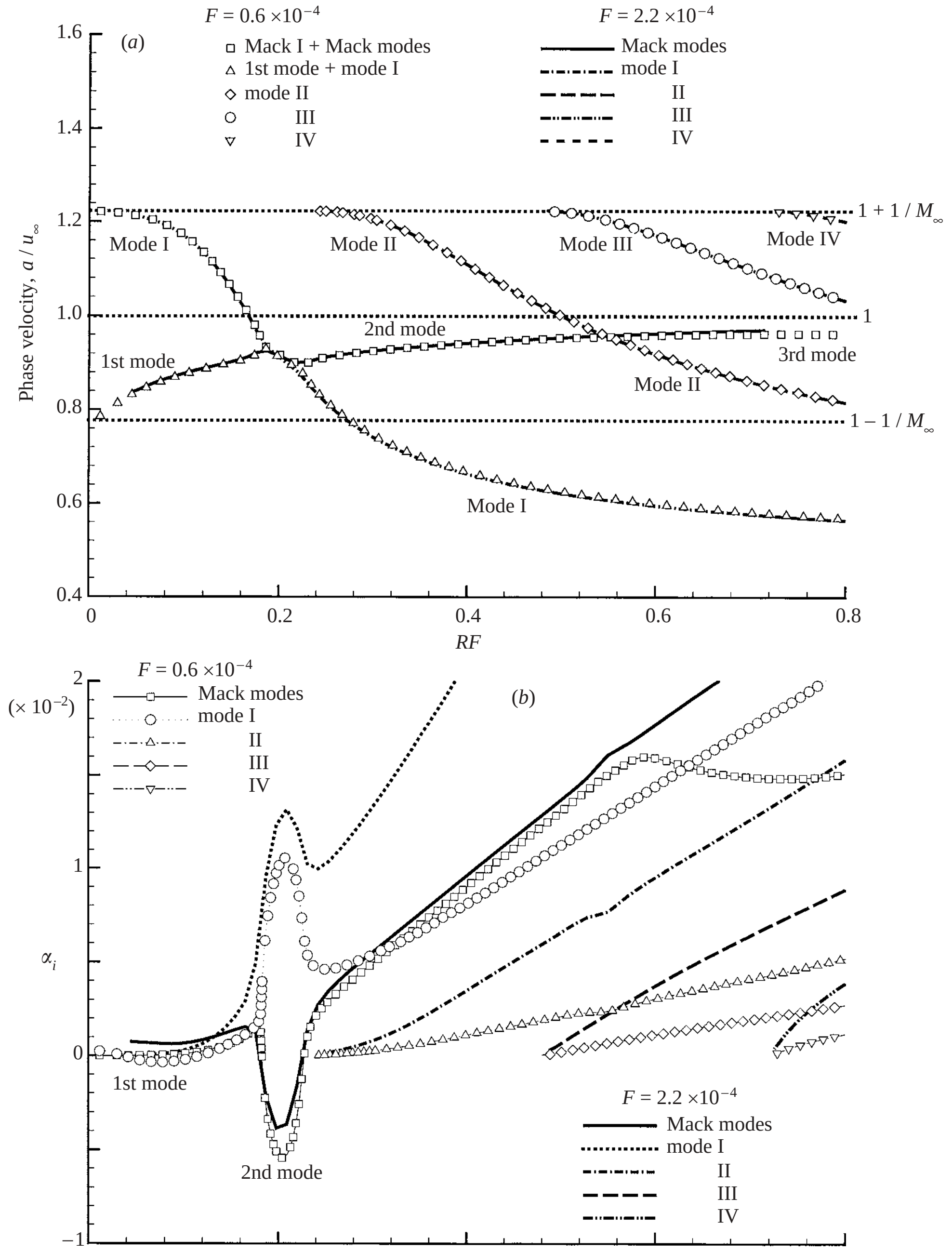

FIGURE 13. (*a*) Phase velocities and (*b*) growth rates of boundary-layer normal modes at different frequencies.

across the boundary layer (figure 14). Such similarity in mode structures also exists between mode II and the Mack mode when they are synchronized with each other (see figure 9). In addition, figure 14 also shows that the structures of the same normal modes for the different frequencies are almost the same at the synchronization point.

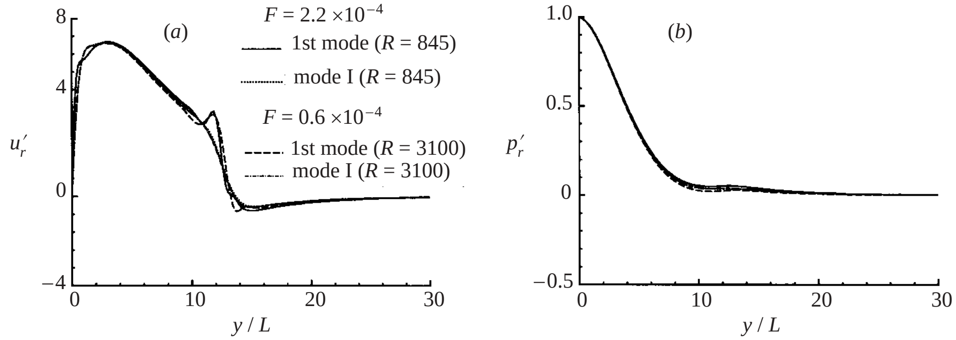

FIGURE 14. Similarity of mode I and the first mode at their synchronization points at two different frequencies ($M_\infty = 4.5$ and $Re^*_\infty = 7.2 \times 10^6\,\mathrm{m}^{-1}$).

Almost the same profiles of normal modes for the different frequencies at different locations can be obtained only if the product of RF is the same.

Figure 13(*b*) also shows the growth rates of different normal modes. For the case of a fixed frequency at $F = 0.6 \times 10^{-4}$, the first mode is unstable. The unstable first mode converts to a stable mode I when it propagates downstream. Meanwhile, the stable mode I converts to an unstable second mode during propagation. The second-mode unstable range of RF is between 0.18 and 0.23 for both the $F = 0.6 \times 10^{-4}$ and $F = 2.2 \times 10^{-4}$ cases. The conjugation between the second mode and mode I is shown in this figure for both cases. Qualitatively, modes I, II, III and IV are stable for both low-frequency and high-frequency cases, although they are more stable for the high-frequency case.

7. Numerical simulations

Having obtained steady base flow solutions and linear stability characteristics of boundary-layer normal modes for the Mach 4.5 flow over a flat plate, extensive unsteady flow simulations are carried out to study the receptivity of the boundary layer to various forcing waves. The numerical simulations are based on solving the full Navier–Stokes equations, which are able to capture in the solutions, the non-parallel effects of the boundary layer, the resonant interactions between different wave modes, and the effects of the oblique shock on the wave modes. The amplitudes of forcing disturbances are carefully chosen so that the non-dimensional amplitudes of the perturbations are at least one order of magnitude larger than that of the maximum numerical noise, and they are small enough to preserve the linearity of boundary-layer disturbances. Numerical tests have demonstrated the linearity of boundary-layer disturbances studied in this paper. Similar results have been shown in Ma & Zhong (2000). In this paper, discrete linear wave modes are introduced from the inlet of the computational domain. The numerical studies of this paper are focused on the wave mode characteristics and the resonant interactions between the Mack mode and the family of stable modes of mode I, mode II, etc. In addition, the effect of frequencies and wall boundary conditions on the boundary-layer disturbances are also investigated.

For each case of the boundary-layer response to a forcing wave, the unsteady computations are carried out until the numerical solutions reach a periodic state. After that, unsteady computations are conducted for one additional period in time, so that a temporal Fourier analysis is performed on the results of the unsteady flow to obtain the amplitudes and phase angles of disturbances in the following form:

$$\phi'(x, y, t) = |\phi'(x, y)| \exp[\mathrm{i}(\psi'(x) - \omega t)]. \tag{13}$$

From the wave amplitudes and phase angles computed by (13), streamwise wavenumbers and growth rates of the disturbance waves can be extracted from the numerical solutions near the wall by

$$\alpha_r = \frac{\mathrm{d}|\psi'|}{\mathrm{d}x}, \tag{14}$$

$$\alpha_i = -\frac{1}{|\phi'|}\frac{\mathrm{d}|\phi'|}{\mathrm{d}x}. \tag{15}$$

The values calculated by using (14) and (15) correspond to the streamwise wavenumber and growth rate of a single wave if the numerical solutions are dominated by a single discrete wave mode in a local region. If the numerical solutions contain a mixture of two or more wave modes, the α_r and α_i are a result of a modulation of these wave modes.

7.1. *Forcing waves from inlet*

The first case is the response of supersonic boundary layer to forcing waves imposed at the inlet. The purpose of the numerical studies is to study the wave modes characteristics and resonant interactions in the supersonic boundary layer. The profiles of the forcing waves at the inlet are specified as those obtained from the LST. At the inlet boundary of the computational domain, the flow is specified as the superposition of the steady base flow and a temporal fluctuations of flow variables at frequency ω, amplitude ϵ, and streamwise wavenumber α_r, i.e.

$$\phi(x_{in}, y, t) = \bar{\phi}(x_{in}, y) + \epsilon\hat{\phi}(y) \exp[\mathrm{i}(\alpha_r x_{in} - \omega t)], \tag{16}$$

where $\phi(x_{in}, y, t)$ represents any of the flow variables. For a given wave mode at a fixed frequency, the wavenumber α_r and the disturbance structure contained in $\hat{\phi}(y)$ is obtained from the LST results. Because x_{in} is fixed at the inflow, the product of $\alpha_r x_{in}$ is a constant for a given α_r. This constant can only affect the phase angle at the inflow. Therefore, it is not necessary to specify α_r when a normal mode is introduced at the inlet. The subsequent downstream propagation of this wave mode and its interactions with other modes are simulated by time-accurate computations of the full Navier–Stokes equations.

7.1.1. *Development of Mack modes in boundary layer*

Neutral stability curves of the Mack modes. It was shown that, among all the normal modes, only the Mack modes can become unstable in the supersonic boundary layer by the LST in § 6. The neutral stability curves of the Mack modes are calculated by using the base flow solution from the numerical simulation. The isothermal wall boundary condition is used for temperature perturbations. Figure 15 shows the neutral stability curves of the first and second modes for the Mach 4.5 flat-plate boundary layer. As the Mack-mode wave at a fixed high frequency ($F = 2.2 \times 10^{-4}$, for example) propagates from upstream to downstream, it goes through a stable region of decay first, then a narrow second-mode unstable region of growth, followed by a stable region again afterward. The second-mode unstable region for a fixed frequency of $F = 2.2 \times 10^{-4}$ predicted by the LST is located in an interval from $R = 806$ (branch I neutral stability point) to 999.6 (branch II neutral stability point). This figure also

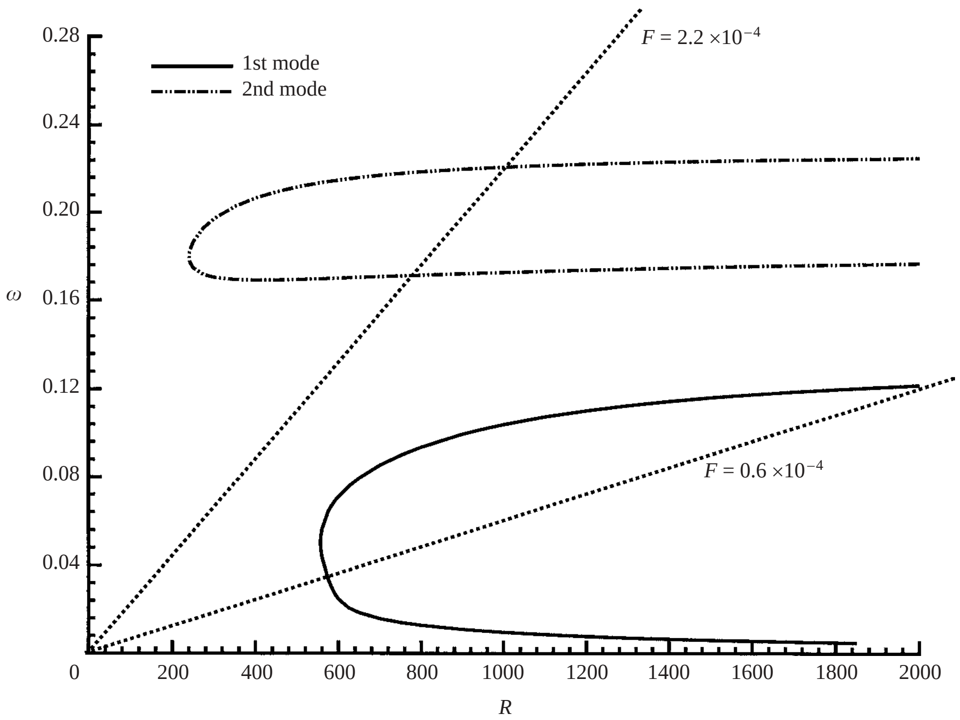

FIGURE 15. Neutral stability curves (ω *vs.* R) of two-dimensional first and second modes in the supersonic boundary layer ($M_\infty = 4.5$ and $Re^*_\infty = 7.2 \times 10^6\,\mathrm{m}^{-1}$).

shows that the second-mode neutral stability points (branch I and branch II) are almost constant in term of ω when either R or F is large. For the second-mode branch I neutral stability points, ω increases from 0.169 to 0.176 when F decreases from 4.84×10^{-4} to 8.83×10^{-5}. The difference is less than 4.0%. For the second-mode branch II neutral stability points, ω increases from 0.215 to 0.225 when F decreases from 3.53×10^{-4} to 1.12×10^{-4}. The difference is less than 4.5%. Therefore, for the Mack-mode neutral stability points (branches I and II), the linear stability curves can be approximately scaled by a single non-dimensional parameter ω ($\omega = RF$) when either R or F is large.

Mack modes at $F = 2.2 \times 10^{-4}$. In this case, the disturbances of a Mack mode with a fixed frequency of $F = 2.2 \times 10^{-4}$ are introduced at the inlet located at $x^* = 0.025\,\mathrm{m}$ ($R = 424.26$ and $RF = 0.0933$). The wave amplitude imposed at the inlet is $|p'|/p_\infty = 0.0002835$. For the same steady base flow field, two different unsteady flow fields are computed by using two sets of wall boundary conditions for the temperature perturbations on the wall, i.e. both the adiabatic boundary condition and the isothermal boundary condition for the wall temperature perturbations. The effects of temperature perturbation boundary conditions on the growth rates of boundary-layer wave modes are investigated. The temperature perturbations are set to zero for the isothermal case. On the other hand, the first-order derivative of the temperature perturbations is set to zero for the adiabatic case. At the location of the current inlet ($RF = 0.0933$), figure 7 shows that the Mack mode is in the region of the first-mode wave.

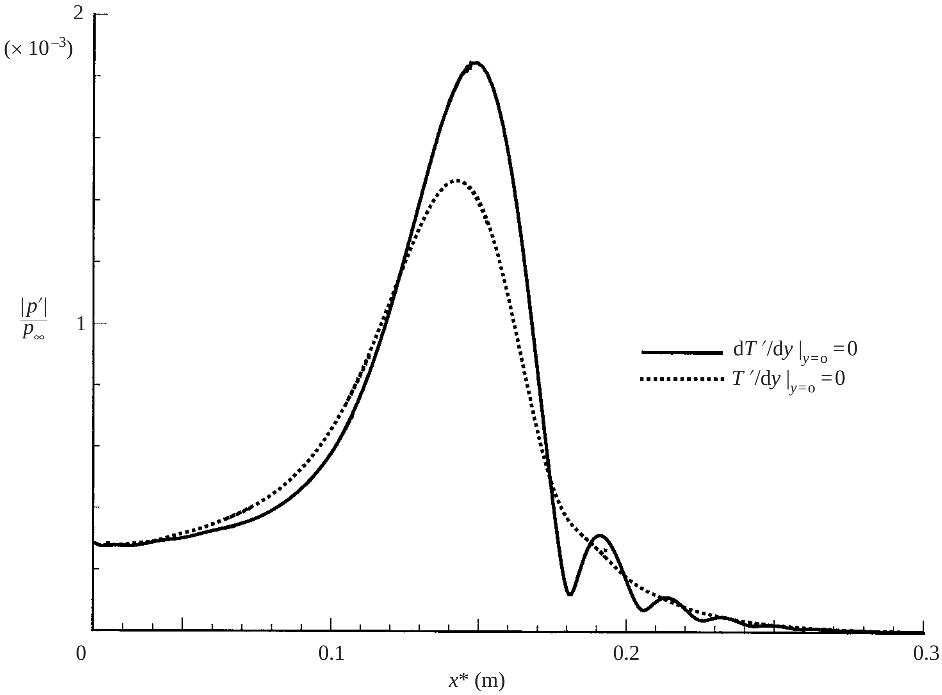

FIGURE 16. Comparison of amplitudes of pressure perturbations along the wall surface for two cases of different boundary conditions for temperature perturbations for the case of an imposed Mack mode at the inlet with $RF = 0.0933$ ($F = 2.2 \times 10^{-4}$).

Figure 16 compares the amplitudes of pressure perturbations along the wall surface between the adiabatic case and the isothermal case after the first mode is introduced from the inlet. It shows that the amplitude of pressure disturbances increases monotonically until it reaches a maximum value at the branch II neutral stability point. After passing the branch II neutral stability point, the amplitudes of the disturbances decay rapidly because the second mode becomes stable. Finally, the amplitudes of the disturbances approach zero further downstream. The figure shows that for the adiabatic case, the branch II neutral stability point is located at $x^* = 0.155$ m (or $R = 1056$) with peak pressure amplitude $|p'|/p_\infty = 0.001845$, which is 6.5 times the pressure amplitude at the inlet. On the other hand, for the isothermal case, the branch II neutral stability point is located at $x^* = 0.142$ m (or $R = 1011$) with peak pressure amplitude $|p'|/p_\infty = 0.001465$, which is 5.2 times the pressure amplitude at the inlet. If the adiabatic wall boundary condition is used for the temperature perturbations, the second-mode unstable region predicted by the LST is from $R = 840$ to $R = 1030.5$ for a fixed frequency of $F = 2.2 \times 10^{-4}$. Therefore, in the simulation of both the adiabatic case and the isothermal case, there is good agreement between the locations of the branch II neutral stability points predicted by the LST and that obtained by numerical simulation based on the full Navier–Stokes equations. Compared with the isothermal case, the maximum amplitude for pressure perturbations is larger for the adiabatic case, which indicates that the second mode is more unstable for the adiabatic case. This is consistent with the LST predictions on the Mack mode growth rates shown in figure 12(*b*). Figure 16 also shows that there is modulation on the amplitude of pressure perturbations after the second mode passes the branch II neutral stability point and becomes stable for the adiabatic case, while pressure perturbations monotonically decay to zero after the branch II neutral stability point for the isothermal case.

The streamwise local wavenumbers α_r and growth rates α_i of the numerical solutions can be calculated, based on pressure disturbances on the wall, by using (14) and (15), respectively. Figure 17 compares the local wavenumbers and growth rates of the disturbances obtained from the numerical simulations with those predicted by the LST based on the same mean flow. The figure shows that streamwise wavenumbers predicted by the LST are the same for the two sets of wall temperature boundary conditions. The wavenumbers computed by the simulations agree well with those predicted by the LST analysis, except in the downstream region for the adiabatic case. The disagreement is because α_r does not represent the wavenumber of the Mack mode in the region when the numerical solutions are a mixture of two or more wave modes. In the numerical solutions for the adiabatic case, there is a modulation between the Mack mode and another mode after passing the branch II neutral stability point. As a result, there is an oscillation for streamwise wavenumbers after that point. However, such a modulation does not exist in the isothermal case. Therefore, there is good agreement on streamwise wavenumbers between the LST and the numerical simulation in isothermal case.

Figure 17 also compares the growth rates between the results obtained from numerical simulations based on (15) and those predicted by the LST. As shown in figure 17, the second mode unstable region based the simulation results is from the beginning to $x^* = 0.142$ m for the isothermal case and to $x^* = 0.155$ m for the adiabatic case. The second-mode branch I neutral point does not show in the simulation results. The peak growth rates predicted by the LST are -0.00256 and -0.00365 for the isothermal case and the adiabatic case, respectively, while the corresponding values obtained from the numerical simulations are -0.00318 and -0.00410, respectively. Both the LST and the simulation results show that the adiabatic case is more unstable than the corresponding isothermal case. In addition, there is a great difference between the growth rates obtained from the numerical simulations and the LST. Specifically, the LST consistently underpredicts the instability of the Mack modes. This trend is true for all test cases we have considered. The numerical simulations account for the effect of the non-parallel boundary layer and the effect of the oblique shock interactions. In the current case, the effect of the shock is negligible because the Mack-mode waves are confined in the boundary layer. Therefore, the difference in the growth rates between the numerical solutions and the LST may be due to the parallel mean flow assumption used in the LST. Overall, there is good agreement in eigenvalues between the LST and DNS. Such agreement is also obtained in comparison of eigenfunction profiles, which is not shown here.

Effect of frequency. The effects of wave frequency on the propagation of the Mack modes are studied by comparing the results of four cases with different frequencies, i.e.

$$F = 2.2 \times 10^{-4}, \quad 1.6 \times 10^{-4}, \quad 1.2 \times 10^{-4}, \quad 0.6 \times 10^{-4}. \tag{17}$$

The adiabatic boundary condition is used for the temperature perturbations on the wall for these computational cases. Figure 18 compares amplitudes of pressure perturbations on the wall for the four cases with different frequencies when the Mack-mode waves with the same initial pressure amplitude of $|p'|/p_\infty = 0.0002835$ are imposed at the inlet. The inlet of the four cases has the same location of

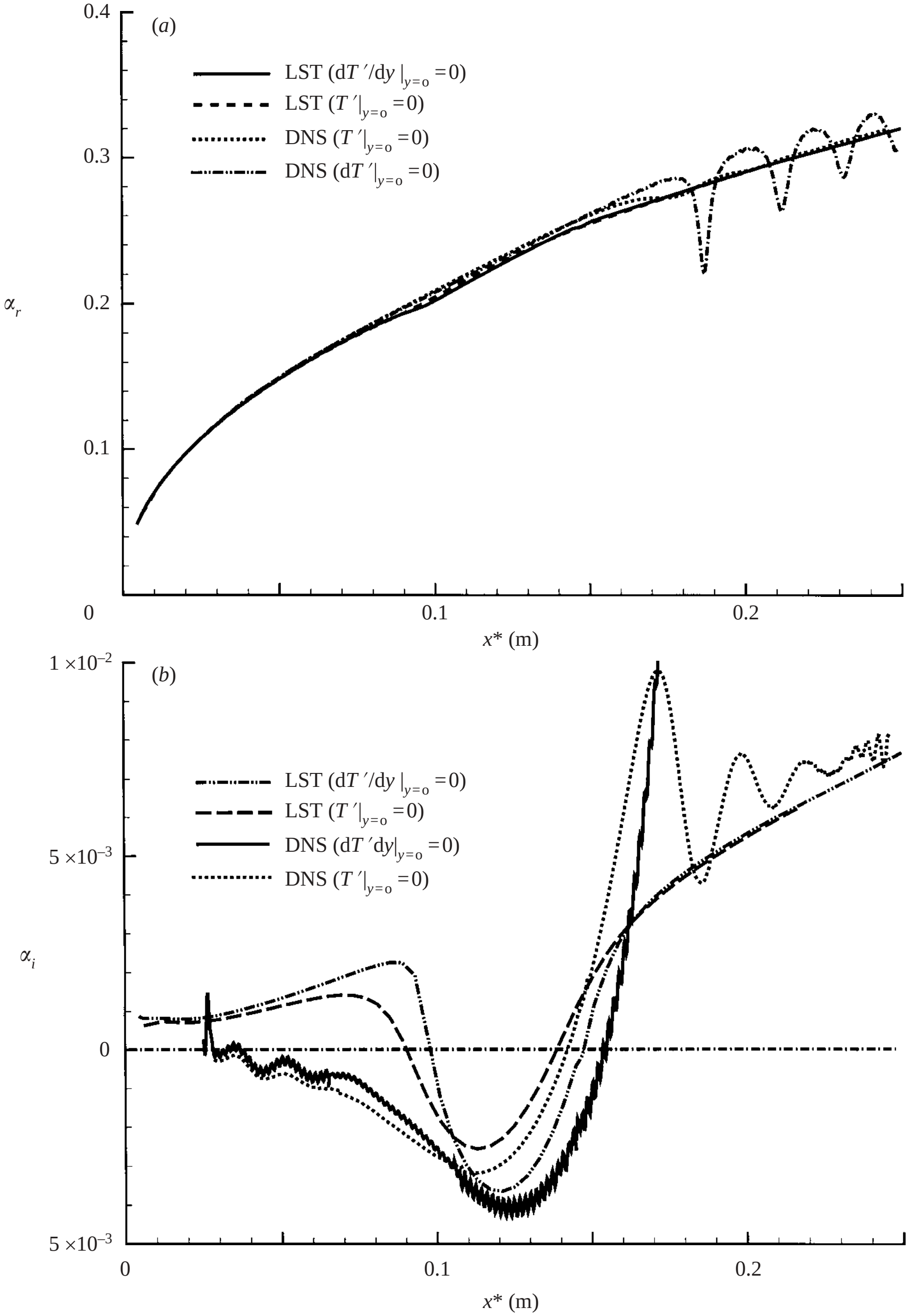

FIGURE 17. Comparison of (*a*) the streamwise wavenumbers and (*b*) the growth rates obtained by numerical simulations and by the LST calculations for the case of an imposed Mack mode at the inlet with $RF = 0.0933$ ($F = 2.2 \times 10^{-4}$).

$x^* = 0.025\,\mathrm{m}$ ($R = 424.26$), where the Mack mode is in the first mode region. The figure shows that as the frequencies decrease, the growth rates of the Mack mode increase and the locations of branch II neutral stability points move downstream.

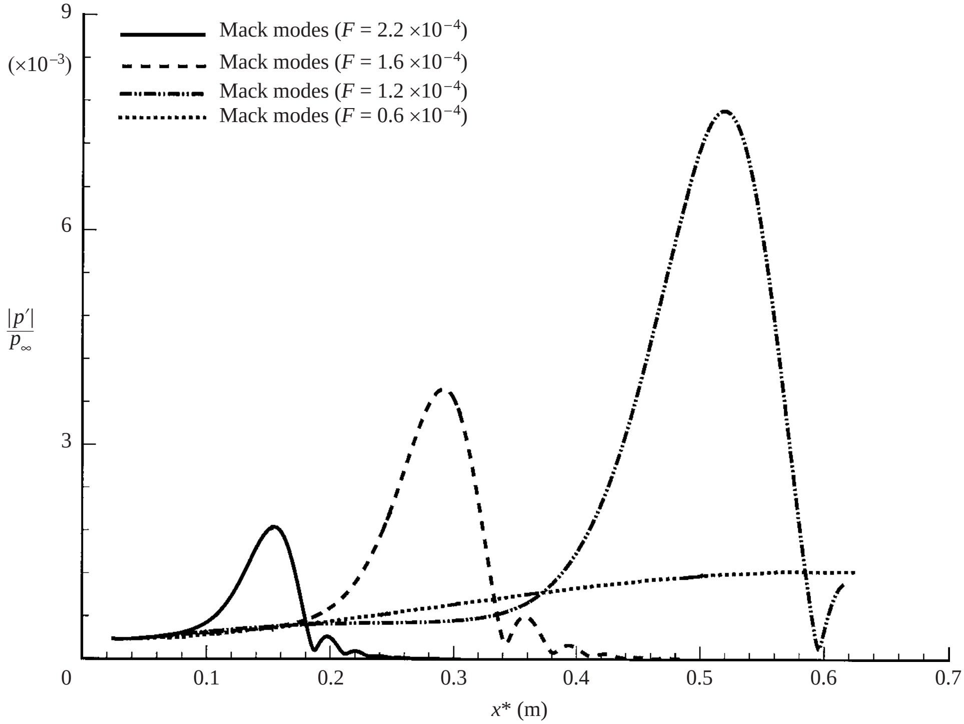

FIGURE 18. Distributions of amplitudes of pressure perturbations of the Mack mode at different frequencies.

The effects of frequencies on the growth rates and the locations of branch II neutral stability points are consistent with the LST prediction. Based on the LST prediction, the locations of the branch II neutral stability point of the second mode in terms of RF are the same for cases of different frequencies (figures 13(*a*) and 15). The peak amplitude of pressure perturbations at the branch II neutral stability point for the case of $F = 2.2 \times 10^{-4}$ is located at $x^* = 0.155$ m, or $RF = 0.2324$ ($R = 1056$). Therefore, it is expected that the peak amplitudes of pressure perturbations for the cases of $F = 1.6 \times 10^{-4}$ and $F = 1.2 \times 10^{-4}$ should be located at $RF = 0.2324$ also, i.e. $R = 1452.6$, or $x^* = 0.293$ m for the case of $F = 1.6 \times 10^{-4}$, and $R = 1936.7$ or $x^* = 0.521$ m for the case of $F = 1.2 \times 10^{-4}$. From the numerical simulation with $F = 1.6 \times 10^{-4}$, the peak amplitude of the pressure perturbation is $|p'|/p_\infty = 0.003774$ and located at $x^* = 0.2914$ m ($R = 1448.5$). For the case of $F = 1.2 \times 10^{-4}$, the peak amplitude of the pressure perturbation is $|p'|/p_\infty = 0.007658$ and it is located at $x^* = 0.5188$ m ($R = 1932.7$). Therefore, the locations of the peak pressure amplitudes from the numerical simulations are consistent with those predicted by the LST.

On the other hand, the peak value of the pressure perturbations for the case of $F = 1.2 \times 10^{-4}$ is almost quadruple that of the case of $F = 2.2 \times 10^{-4}$ and twice that of the case of $F = 1.6 \times 10^{-4}$. This can be explained from the LST prediction on the growth rates of the second mode. For different frequencies, there are very similar growth rate curves in the second-mode unstable region in terms of RF shown in figure 13(*b*). RF is proportional to the square root of physical length x^* for a fixed frequency. For different frequencies, the second-mode unstable region expressed in x^* should be longer for the lower-frequency case given the same range of RF. From

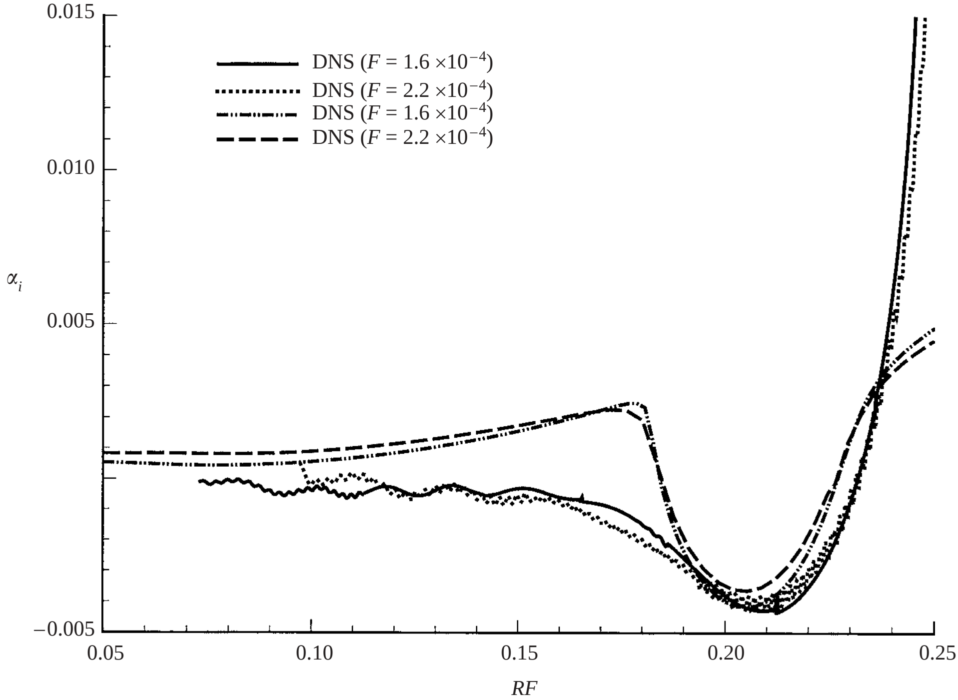

FIGURE 19. Comparison of the growth rates of the Mack mode between the LST and simulation results for two sets of frequencies: $F = 2.2 \times 10^{-4}$ and $F = 1.6 \times 10^{-4}$.

the definition of growth rates (equation (15)), the amplitude changing with x can be obtained by taking integration of growth rates with respect to x^* according to the following formula:

$$|\phi'|(x^*) = |\phi'_0| \exp\left(\int_{x_0^*}^{x^*} -\alpha_i(\omega)\,\mathrm{d}x^*\right), \tag{18}$$

where ω is a function of x^*, and $|\phi'_0|$ is the initial wave amplitude at x_0^*. Therefore, a longer integration range in the second-mode unstable region leads to larger disturbance amplitudes for the cases of lower frequency given the same initial wave amplitudes.

For the case with $F = 0.6 \times 10^{-4}$, the unstable region of the second mode is out of the range of the current computational domain ($0.02592 < RF < 0.128$), while the first mode is slightly unstable from the LST prediction, as shown in figure 13(*b*). The LST prediction agrees with the simulation results, as shown in figure 18. The first-mode branch II neutral stability point from the LST is located at $x^* = 0.536$ ($R = 1963.6$). From simulation, pressure perturbations reach a peak value of $p'/p_\infty = 0.001226$ at $x^* = 0.573$ ($R = 2031.16$). The numerical solutions agree well with those of the LST prediction in terms of the location of the branch II neutral stability point for the first mode.

Figure 19 compares the growth rates as a function of RF between the results from LST and numerical simulations for two cases of different frequencies, i.e. $F = 2.2 \times 10^{-4}$ and 1.6×10^{-4}. Again, the growth rate curves obtained from the numerical simulations for two cases of different frequencies are very close to each other, except that the peak

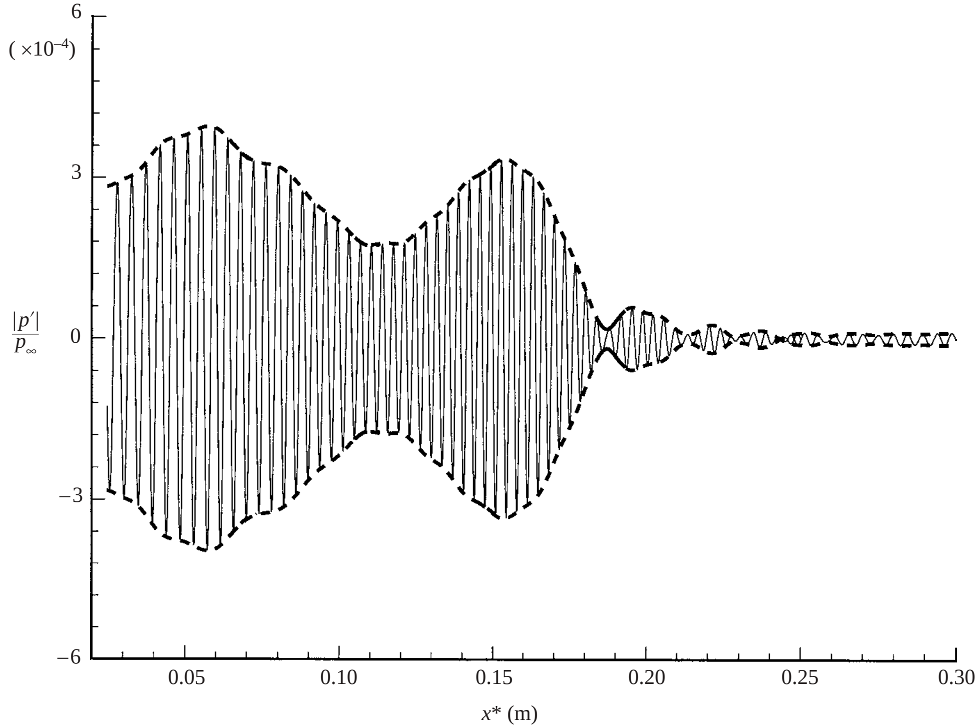

FIGURE 20. Distribution of instantaneous pressure perturbations along the wall surface ($F = 2.2 \times 10^{-4}$).

growth rate is slightly larger for the case of $F = 1.6 \times 10^{-4}$. The locations of the peaks at different frequencies are approximately the same. Therefore, both the results from the the LST predictions (figuers 10 and 13*b*) and those from numerical simulations (figure 19) show that the growth rate curves of the second mode *vs.* RF are very close for different frequencies. As discussed before, compared with the numerical solutions, the corresponding LST results underpredict the growth rates of the second mode in the supersonic boundary layer.

Therefore, the results predicted by the LST are accurate in predicting the wavenumbers and wave mode structures of the Mack modes in the supersonic boundary layer, but the LST results are not accurate in predicting the growth rates of the Mack modes. The LST calculations consistently underpredict the growth rates as compared with the full Navier–Stokes simulations.

7.1.2. *Mode I propagation and resonant interactions with Mack modes*

Mode I at $F = 2.2 \times 10^{-4}$. The development of mode I waves in the boundary layer is considered in this section, where forcing disturbances of mode I with a frequency of $F = 2.2 \times 10^{-4}$ are introduced at the inlet of the computational domain located at $x^* = 0.025\,\mathrm{m}$ ($R = 424.26$).

Figure 20 shows the instantaneous pressure disturbances along the wall surface after the unsteady solutions reach a periodic state. The adiabatic wall boundary condition is used for temperature perturbations. Compared with the results of a single Mack mode propagation shown in figure 16, the wave patterns induced by a mode I wave at the inlet are more complicated. There are multiple peaks in amplitudes of pressure perturbations, which indicate the excitation of different wave modes at different locations during the wave propagation from the inlet to the downstream area. The amplitudes of pressure disturbances increase before reaching the first peak located approximately at $x^* = 0.06\,\mathrm{m}$, which means this mode is unstable in this region. This is contradictory to the LST prediction shown in figure 10 that mode I should always be stable. Intuitively, the amplification of mode I may be due to the effect of the shock wave, which is not included in the LST. A similar numerical simulation on the propagation of mode I is performed by using a rectangle domain without the shock wave and boundary-layer self-similar solutions are used as inflow conditions (Ma & Zhong 2000). The results show that the effect of the shock on the propagation of mode I disturbances in the boundary layer is negligible. One possible reason is that the amplification of mode I results from the interaction between mode I waves and other waves in the flow field, which will be discussed further in § 7.1.3.

After passing the first peak (at $x^* = 0.06\,\mathrm{m}$), mode I waves decay owing to its inherent stable property. Figure 20 show a second growth region for mode I in the range of x^* between 0.115 and 0.155 m. This growth results from the instability of the second Mack mode. As shown in figure 7, mode I and the first mode become synchronized at the synchronization point. Furthermore, both the first mode and mode I have almost the same profiles of disturbances across the boundary layer at the synchronization point (figure 9). As a result, mode I waves convert to the Mack-mode waves in the synchronization region. In fact, the wave mode exchange between mode I and the Mack mode has been discussed in § 6 (figure 13*a*). After the synchronization point between mode I and the first mode, the Mack mode becomes the second mode, which is unstable in the region closely behind the synchronization point. The wave amplitudes in the region after the synchronization point increase because of the growth of the induced second mode in its unstable region. Therefore, the boundary-layer disturbances obtained by the numerical simulation are amplified again when they reach the second-mode unstable region.

The process through which mode I waves convert to the second mode waves is also shown in the distribution of the phase velocities calculated from the numerical solutions of the pressure disturbances along the wall surface as shown in figure 21. The figure shows that the phase velocities obtained from the simulation are the same as those of mode I predicted by the LST in the upstream region. This is expected because the disturbances imposed at the inlet are those of mode I obtained from the linear stability analysis. As the wave propagates downstream, mode I converts to the first mode at the wave synchronization point between mode I and the Mack mode located at approximately $x^* = 0.1\,\mathrm{m}$. After the synchronization point, the second mode induced by mode I propagates downstream. The amplitudes of the second Mack mode grow in the subsequent unstable region until it reaches the branch II neutral stability point. After the Mack-mode waves pass the branch II neutral stability point of the second mode, the amplitudes of the disturbances decay rapidly in the second-mode stable region. There are strong oscillations in the phase velocity distribution after the decay of the second mode because the disturbances result from the modulation of the second mode and other modes.

These results indicate that although mode I is always stable, it can play an important role in the receptivity process because it can convert to the unstable Mack mode through the resonant interaction with Mack modes. The amplitudes of the induced Mack mode can grow in its unstable region immediately following the wave synchronization point.

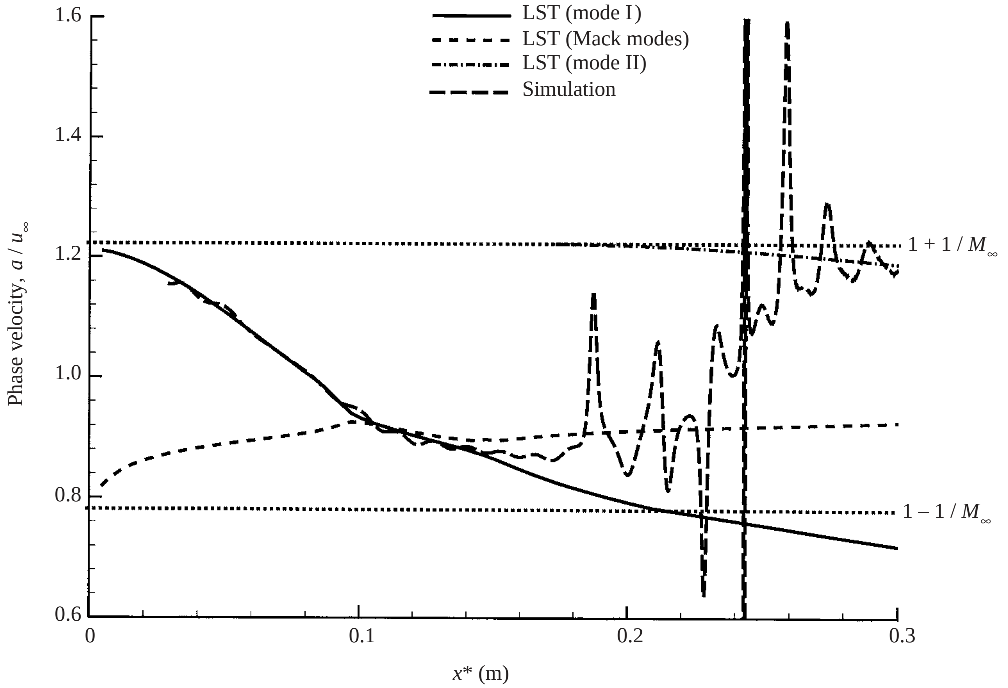

FIGURE 21. Comparison of the phase velocities between the results from the LST predictions and those from numerical solutions based on pressure disturbances on the wall ($F = 2.2 \times 10^{-4}$).

Effect of frequency. The effect of frequency on mode I propagation and interaction with the Mack modes in the boundary layer is studied by comparing the numerical simulation results of four test cases of different frequencies:

$$F = 2.2 \times 10^{-4}, \quad 1.6 \times 10^{-4}, \quad 1.2 \times 10^{-4}, \quad 0.6 \times 10^{-4}. \tag{19}$$

Similar to the previous case, the disturbances of a single mode I wave, of the same amplitude but different frequencies, are imposed at the inlet. The adiabatic boundary condition is used for the temperature perturbations on the wall for all four cases. Again, though mode I is predicted to be always linearly stable by the LST for all four frequencies, the imposed mode I waves can excite the second Mack mode waves through resonant interactions.

Figure 22 compares the amplitudes of the pressure perturbations on the wall for the four cases of different wave frequencies when mode I waves are introduced at the same inlet location of $x^* = 0.025$ m ($R = 424.26$). The initial pressure amplitudes are the same for all cases at $|p'|/p_\infty = 0.0002835$. The figure shows that the amplitudes of pressure disturbances for these cases of different frequencies increase at the beginning due to the interaction between mode I disturbances and other modes. After reaching the first peak values, the amplitudes of pressure disturbances decrease owing to the inherent stable characteristic of mode I. After passing the first peaks in amplitudes, unstable second-mode waves are induced by mode I waves at the wave synchronization points. The amplitudes of the second mode grow significantly in its unstable region before reaching the second peaks of the disturbance amplitudes at the second-mode branch II neutral stability points. After passing branch II neutral stability points, both mode I and the second-mode waves die down because both waves are stable.

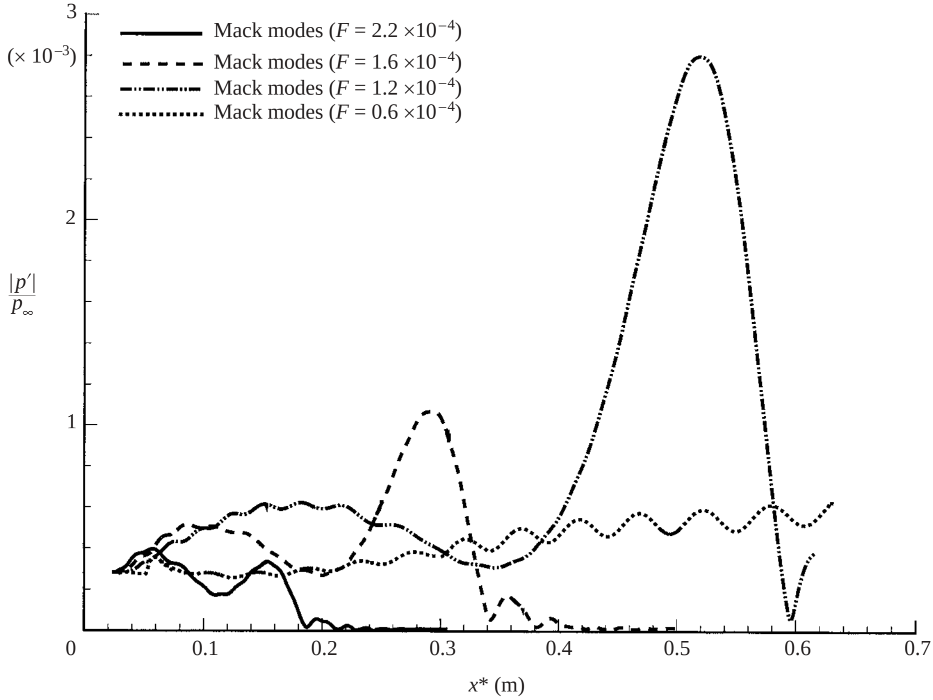

FIGURE 22. Distributions of the amplitudes of pressure perturbations on the wall for the cases of imposed mode I of different frequencies at the inlet.

The peak values at the second-mode branch II neutral points are 0.0003346, 0.001068 and 0.002797, for the cases of $F = 2.2 \times 10^{-4}$, $F = 1.6 \times 10^{-4}$ and $F = 1.2 \times 10^{-4}$, respectively, which are 1.18, 3.77 and 9.87 times their initial amplitudes at the inlet. For the case of $F = 0.6 \times 10^{-4}$, the region of instability of the second mode is located further downstream, which is outside the computational domain considered in this paper.

Effect of wall temperature boundary conditions. The effect of the wall temperature boundary conditions on the propagation of mode I is investigated by introducing mode I disturbances at the inlet with both the isothermal wall and the adiabatic wall boundary conditions. The inlet is located at $x^* = 0.025$ m ($R = 424.26$), and the initial pressure amplitude is $|p'|/p_\infty = 0.0002835$. Two cases with different frequencies of $F = 2.2 \times 10^{-4}$ and $F = 1.2 \times 10^{-4}$ are studied. Figure 23 compares the amplitudes of pressure perturbations on the wall between the cases with two different wall temperature boundary conditions and two different frequencies. Overall, the amplitudes of pressure perturbations away from the inlet are much smaller for the isothermal cases compared to those of the adiabatic cases with the same frequency. Especially, at the same frequency, pressure amplitudes at the second-mode branch II neutral stability points are much smaller in the isothermal case than those in the adiabatic case. The reason for the difference in wave amplitudes between the adiabatic cases and the isothermal cases is that the normal modes of the isothermal cases are linearly more stable than those of the adiabatic cases (figure 12*b*). Compared with an adiabatic case, mode I in an isothermal case is less amplified before it reaches the first peak in pressure perturbations. Furthermore, the amplitudes of mode I disturbances

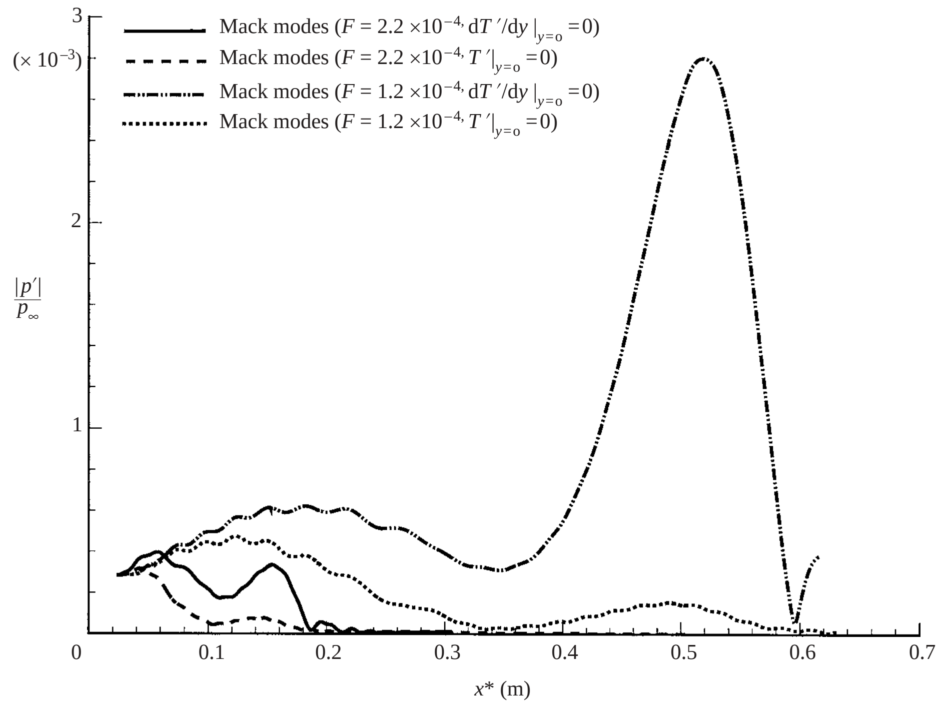

Figure 23. Comparison of the amplitudes of pressure perturbations along the wall surface for mode I with different wall boundary conditions at different frequencies.

in the isothermal case decay much faster and die down to a much smaller value when the wave reaches the synchronization point between mode I and the Mack modes. As a result, the initial amplitudes of the induced second-mode waves are much smaller in the isothermal cases than those in the corresponding adiabatic cases. In addition, the growth rates of the second mode shown in figure 12(*b*) are smaller for the isothermal case than those for the adiabatic case. Therefore, the amplitudes of induced second-mode waves at the branch II neutral stability point are significantly smaller for the isothermal cases than those for the adiabatic cases.

7.1.3. *Mode II propagation and resonant interactions with acoustic waves*

The development of mode II waves in the boundary layer is considered in this section. Similar to mode I, this mode is always stable according to the LST prediction, but the waves are important to the supersonic boundary-layer receptivity process. As shown in figure 7, mode II was initiated at the same phase velocity as that of the free-stream fast acoustic wave at $1 + 1/M_\infty$. As mode II propagates downstream, the phase velocity decreases. Mode II can have an energy exchange with the fast acoustic waves in the boundary layer through these resonant interactions. Such resonant interactions are critical to the receptivity of the Mack mode in the supersonic boundary layer.

The results of two test cases of mode II propagation are presented in this section. In both cases, mode II disturbances of the same frequency are imposed at different inlet locations. In the first case, the initial mode II waves are imposed at $RF = 0.3552$. Figure 7 shows that the inlet location in this case is downstream of the location where mode II first appears. On the other hand, in the second case, the initial mode II waves are imposed at $RF = 0.2539$. The inlet location is near the location of the

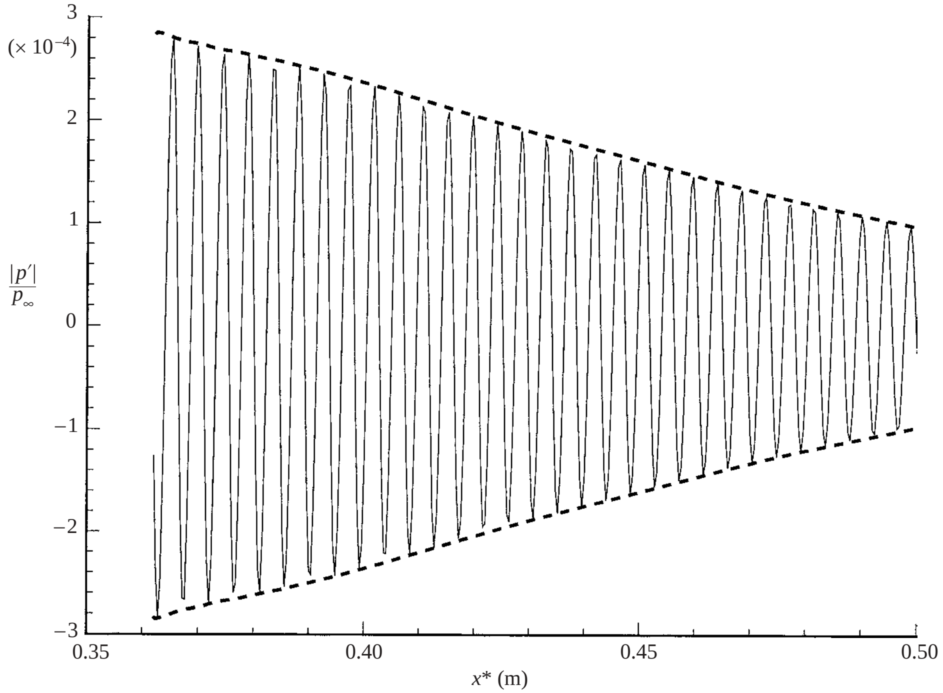

FIGURE 24. Distribution of instantaneous pressure perturbations of mode II propagation along the wall surface for the case of imposed mode II at inlet with $RF = 0.3552$ ($F = 2.2 \times 10^{-4}$).

first appearance of mode II. The results in this case will show that the subsequent development of mode II is very different in these two cases because there are wave interactions near this synchronization point between mode II and the fast acoustic waves.

Mode II of $F = 2.2 \times 10^{-4}$ *imposed at the inlet with* $RF = 0.3552$. In this case, the forcing disturbances of mode II with a frequency of $F = 2.2 \times 10^{-4}$ are introduced at the inlet of the computational domain located at $x^* = 0.362$ m ($R = 1614.43$). The adiabatic wall boundary condition is used for the temperature perturbations on the wall. The inlet is located at $RF = 0.3552$ in the phase velocity plots of figure 7, which shows that mode II is imposed from downstream of its initial synchronization point with the fast acoustic wave.

Figure 24 shows the instantaneous pressure disturbances along the wall surface. The decaying of pressure disturbances indicates that mode II waves are stable, which is consistent with the prediction of the LST (figure 10). This figure shows that the simulation results of this case only contain the disturbances of pure mode II waves in the boundary layer. No other wave modes are excited. As predicted by the linear stability analysis, the wave mode is stable as it propagates downstream. The results of numerical simulations are expected to agree with the LST results because there are no other wave components in the solutions.

Figure 25 compares the profiles of disturbances at $x^* = 0.488$ m ($R = 1874.46$) obtained from the numerical simulation and those predicted by the LST as the eigenfunctions of mode II. The figure shows excellent agreement in the disturbance structures between the numerical results and the LST predictions. Figure 26 shows the comparison of streamwise wavenumbers (α_r) and growth rates (α_i) obtained by

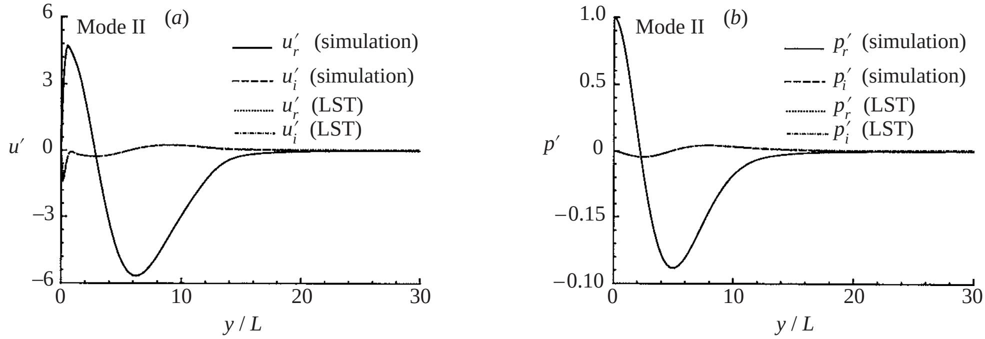

FIGURE 25. Comparison of the wave structure of mode II obtained by the LST and by numerical simulation for grid station located at $R = 1874.46$ for the case of imposed mode II at inlet with $RF = 0.3552$ ($F = 2.2 \times 10^{-4}$).

the numerical simulation and the corresponding values predicted by the LST. The figure shows very good agreement in streamwise wavenumbers. Therefore, there are only pure mode II waves in the boundary layer. The eigenfunctions and wavenumbers of the waves can be predicted well by the linear stability analysis. However, consistent with other modes, the LST analysis overpredicts the growth rates (α_i) of mode II in the boundary layer, as shown in figure 26(*b*). Therefore, there are significant differences for the growth rates between the LST predictions and the numerical simulation results (larger than 50% in maximum). Again, the differences may be because a parallel assumption is used in the linear stability analysis, whereas the actual boundary layer is not parallel. The non-parallel effect becomes stronger at higher Mach numbers.

Mode II of $F = 2.2 \times 10^{-4}$ *imposed at inlet with* $RF = 0.2539$. In this case, mode II disturbances are introduced through the inlet at $x^* = 0.185\,\mathrm{m}$ ($R = 1154.12$). This case is different from the previous case only in the location of the inlet. For the previous case, the inlet is located downstream of the initial synchronization point between mode II waves and fast acoustic waves. For this case, the inlet is located at $R = 1154.12$ ($RF = 0.2539$), which is very close to the synchronization point between mode II waves and fast acoustic waves. The profiles of mode II disturbances at the inlet are showed in figure 27. It shows that the wave structures of mode II at this early location contain strong amplitudes in the region outside the boundary layer.

Figure 28 shows the distribution of instantaneous pressure disturbances along the wall surface. Compared with the previous case of mode II propagation shown in figure 24, figure 28 shows that the disturbance field of the current case contains a mixture of several wave modes with multiple peaks in perturbation amplitudes. Even though mode II is always a stable mode according to the LST analysis, the amplitudes of pressure disturbances along the wall surface for the current case increase before they reach the peak value. However, according to figure 10, mode II is predicted by the LST always to be stable. This difference in the stability result is not because the effect of the shock is neglected in the LST analysis. A similar numerical simulation study on the stability properties of mode II by using a rectangle domain without the shock shows that the effect of the shock on the mode II stability is negligible.

It is found that the amplification of wave amplitudes in a stable region of mode II is caused by a resonance between mode II disturbances and the fast acoustic waves outside the boundary layer. From the profiles of mode II disturbances at the inlet shown in figure 27, the structure of wave disturbances of mode II does not decay

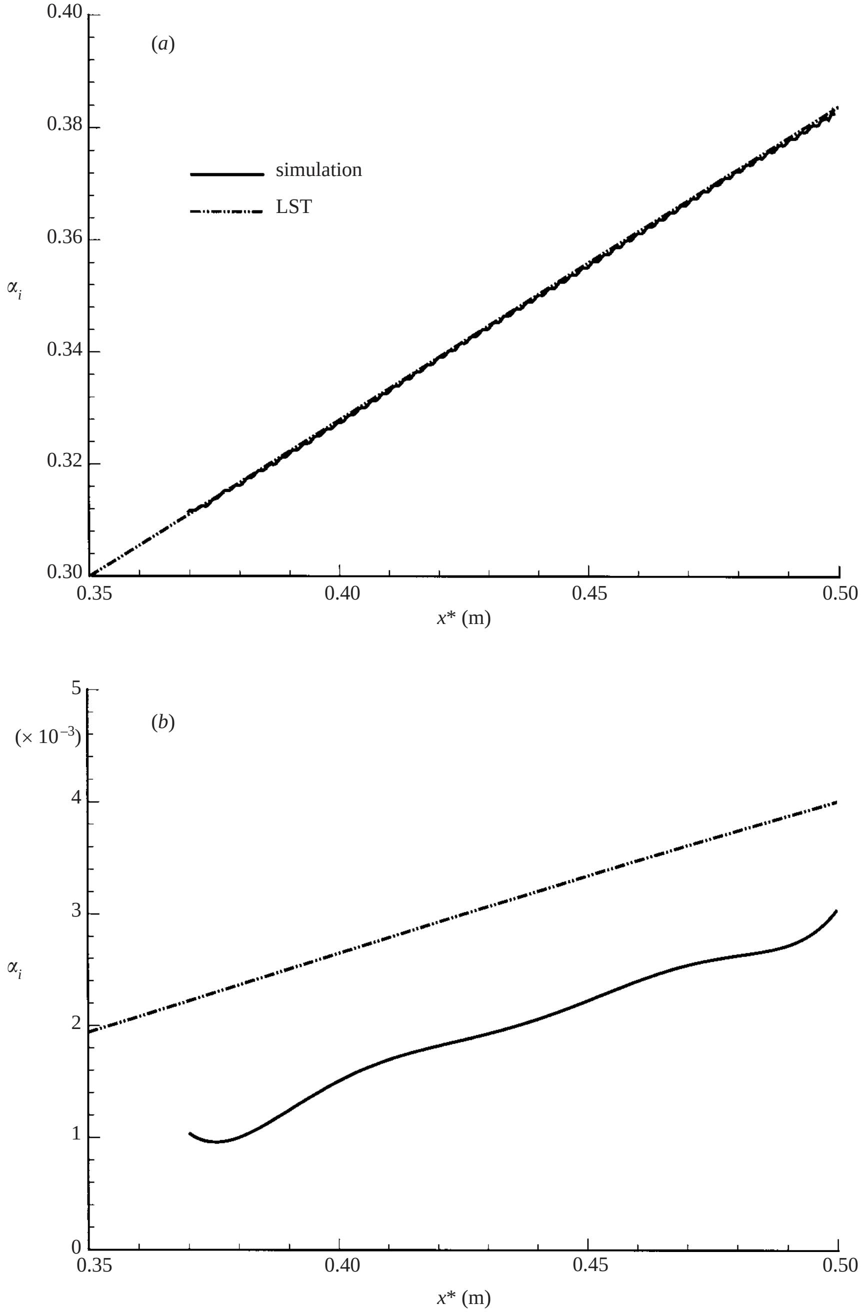

FIGURE 26. Comparison of (*a*) the wavenumber and (*b*) the growth rate distributions of mode II between the simulation and the LST results for the case of imposed mode II at inlet with $RF = 0.3552$ ($F = 2.2 \times 10^{-4}$).

exponentially outside the boundary layer at the synchronization point at the inlet. The mode II wave profiles are very different from those of the same mode at downstream locations (see figure 25) where mode II is not synchronized with the fast acoustic wave. In other words, there are strong disturbances outside the boundary layer for

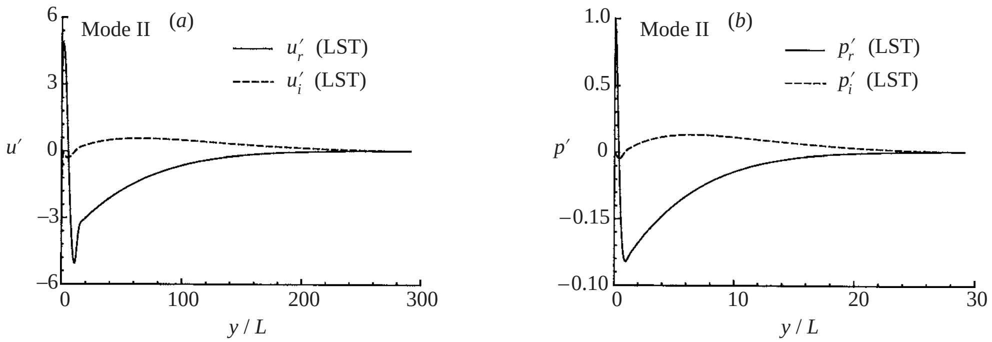

FIGURE 27. Profiles of mode II disturbances obtained from LST at the inlet with $RF = 0.2539$ ($F = 2.2 \times 10^{-4}$).

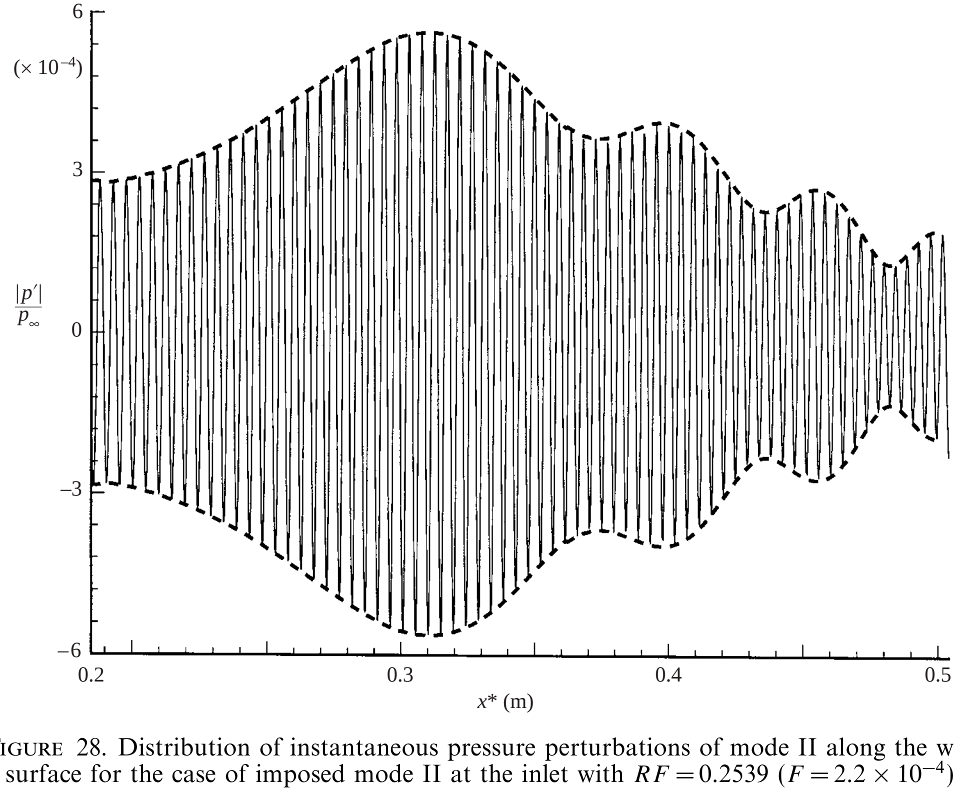

FIGURE 28. Distribution of instantaneous pressure perturbations of mode II along the wall surface for the case of imposed mode II at the inlet with $RF = 0.2539$ ($F = 2.2 \times 10^{-4}$).

mode II near the synchronization point between mode II waves and fast acoustic waves. The disturbances outside the boundary layer belong to fast acoustic waves because the non-dimensional amplitudes of disturbances satisfy the relationship of fast acoustic waves, i.e.

$$\sqrt{|u'|^2 + |v'|^2} = |p'|M_\infty = \frac{|T'|}{M_\infty(\gamma - 1)}. \tag{20}$$

Figure 29 compares the non-dimensionalized magnitudes of the mode II wave at the inlet. The figure shows that the perturbations of mode II outside the boundary layer

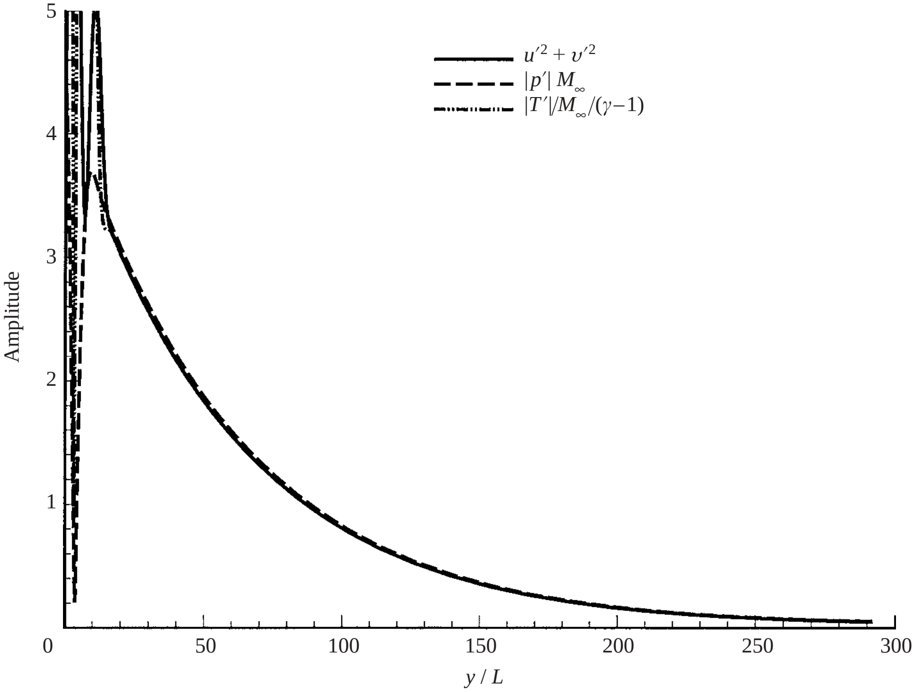

FIGURE 29. Wave structure of disturbances, obtained from LST, imposed at the inlet with $RF = 0.2539$ ($F = 2.2 \times 10^{-4}$).

satisfy the acoustic wave relations given by (20). In addition, the phase velocities of induced disturbances outside the boundary layer are the same as the phase velocity of a fast acoustic wave, i.e.

$$a = 1 + 1/M_\infty. \tag{21}$$

Figure 30 shows the profiles of phase velocities of induced disturbances along the wall-normal direction at different streamwise locations. The phase velocities approach that of a fast acoustic wave in the region outside the boundary layer. The results in both figures 30 and 29 indicate that there are strong acoustic wave components outside the boundary layer in the initial mode II disturbances, which are introduced through the inlet at $x^* = 0.185$ m ($RF = 0.2539$) in the numerical simulation. Figure 30 also shows that the phase velocities of mode II inside the boundary layer decrease as mode II waves propagate downstream.

Figure 31 shows the comparison of phase velocities of mode II predicted by the LST and those obtained by the numerical simulations of imposed mode II with the same frequency at different inlet locations. The figure shows that mode II waves are modulated by the fast acoustic wave when mode II are imposed near their initial wave synchronization location. On the other hand, if mode II are imposed at an inlet downstream of the initial point, there is no wave modulation. The wavenumbers of the numerical simulation for this case (simulation 1) agree very well with those obtained by the LST.

Figure 32 compares the profiles of disturbances at $x^* = 0.488$ m ($R = 1874.46$ and $RF = 0.4124$) obtained from the numerical simulation with those predicted by the LST. The numerical simulation is for the second case of mode II imposed near the

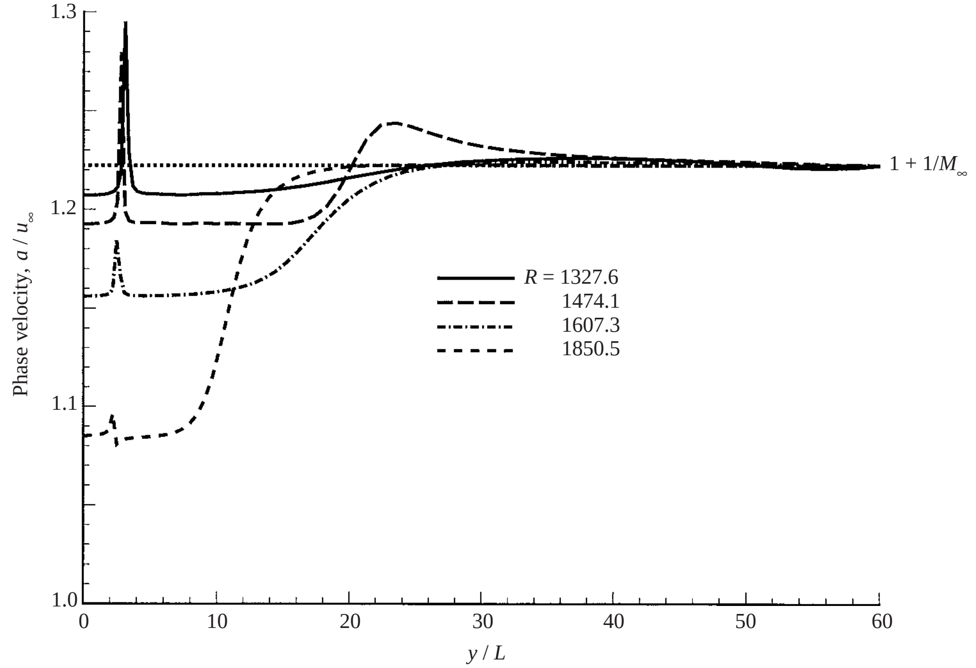

FIGURE 30. Profiles of phase velocities of wave disturbances obtained by numerical simulations for the case of imposed mode II at the inlet with $RF = 0.2539$ ($F = 2.2 \times 10^{-4}$).

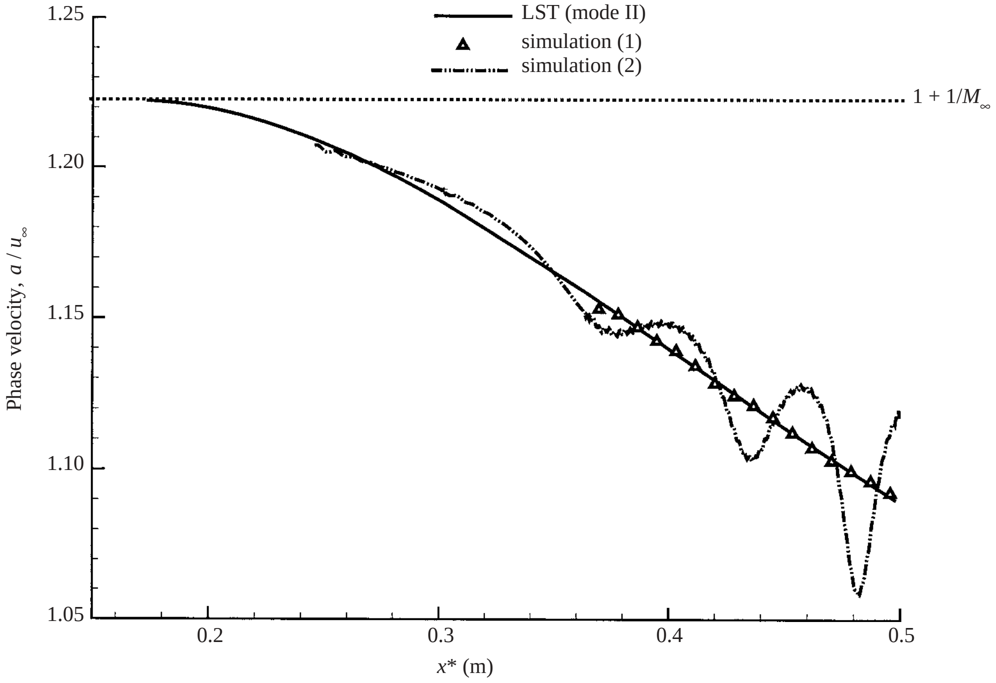

FIGURE 31. Comparison of phase velocities of the LST and those of numerical simulation for mode II disturbances introduced at different inlet locations (simulation 1: $R_{inlet} = 1614.43$, simulation 2: $R_{inlet} = 1154.12$, $F = 2.2 \times 10^{-4}$).

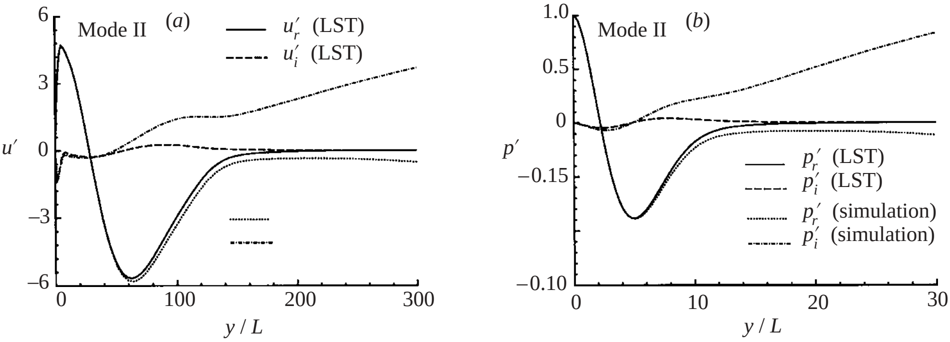

FIGURE 32. Comparison of the wave structure of mode II obtained by the LST and by numerical simulation for grid station located at $R = 1874.46$ for the case of imposed mode II at inlet with $RF = 0.2539$ ($F = 2.2 \times 10^{-4}$).

initial wave synchronization location. The figure shows that there is good agreement in the disturbance structures inside the boundary layer between the numerical simulation solutions and eigenfunctions predicted by the LST. However, because of a modulation of mode II with the acoustic wave in the simulation, the two sets of results do not agree outside the boundary layer. In the numerical simulation, the wave field downstream contains both mode II wave and strong acoustic wave components outside the boundary layer. The acoustic wave is excited by mode II through their mutual resonant interaction. It is expected that an imposed forcing acoustic wave can also excite mode II at this synchronization location through their resonant interactions.

Therefore, the characteristics of mode II propagation in the supersonic boundary layer can be summarized as follows. Figure 7 shows that the phase velocities of mode II waves are the same as those of the fast acoustic waves when mode II waves initially appear in the figure. At this initial location, there is a strong resonant interaction between mode II and the fast acoustic waves, because the phase velocities of mode II disturbances are synchronized with that of the acoustic waves. As a result, though predicted to be stable by the LST, mode II disturbances are amplified when they are introduced at the inlet near this synchronization point located at $RF = 0.2539$. Similarly, the amplification of mode I waves is also due to the resonance between mode I waves and acoustic waves. Since the LST analysis cannot account for the interactions between different types of wave, the amplification of mode II disturbances cannot be predicted correctly by the LST when there are resonant wave interactions. The current numerical simulation approach based on the full Navier–Stokes equations can take account of these interactions, as well as the effect of shock interaction with wave modes. On the other hand, when mode II disturbances are introduced through the inlet at a location further downstream with $RF = 0.3552$, the mode II disturbances are mainly confined inside the boundary layer and all disturbances decay exponentially to zero outside the boundary layer (see figure 25). In addition, downstream after $RF = 0.3552$, the phase velocities of mode II waves are far away from those of the fast acoustic waves as shown in figure 31). Therefore, there is no interaction between mode II waves and the acoustic waves in this case. Consequently, there is good agreement on the wavenumbers of mode II disturbances between the results from the LST and the numerical simulation, though the LST consistently underpredicts the magnitude of the growth rates, owing to the effect of non-parallel boundary layer, which is neglected in the LST.

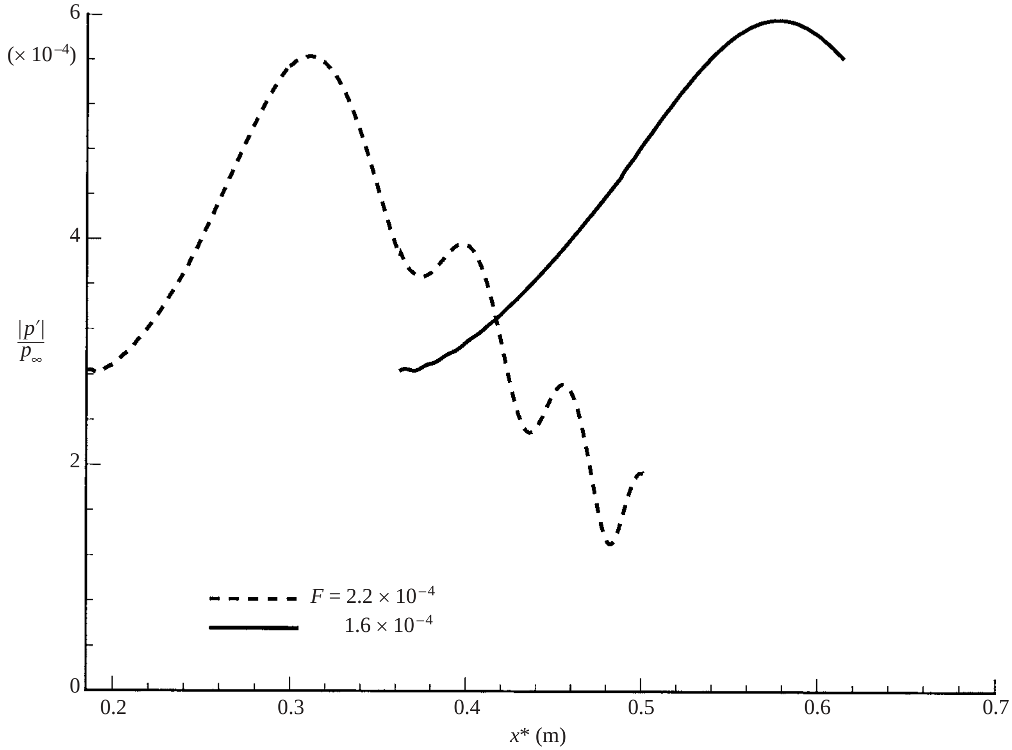

FIGURE 33. Comparison of mode II pressure perturbation amplitudes for two cases of different frequencies.

Effect of frequency. The effect of frequency on the properties of the mode II wave is studied by comparing results of mode II propagation at two different frequencies: $F = 1.6 \times 10^{-4}$ and $F = 2.2 \times 10^{-4}$. The adiabatic wall boundary condition is used for both cases. The mode II disturbances are introduced at the inlet with approximately the same value of RF as in figure 7. For the cases of $F = 1.6 \times 10^{-4}$ and $F = 2.2 \times 10^{-4}$, the inlets are located at $x^* = 0.362$ m ($RF = 0.2583$) and $x^* = 0.185$ m ($RF = 0.2539$), respectively.

Figure 33 compares the amplitudes of pressure perturbations on the wall for the two cases of different frequencies. The figure shows that the amplitudes of pressure disturbances increase at the beginning owing to the resonance between mode II waves and the acoustic waves which are dominant outside the boundary layer. After reaching peak values, the amplitudes of pressure disturbances decay as mode II waves propagate downstream. The inflow condition of pressure disturbances at the inlet is $|p'|/p_\infty = 0.0002835$ for both cases. The peak amplitudes of pressure disturbances are $|p'|/p_\infty = 0.00056295$ and $|p'|/p_\infty = 0.00059570$ for $F = 2.2 \times 10^{-4}$ and $F = 1.6 \times 10^{-4}$, respectively. Unlike the second Mack mode, which is much more amplified for lower frequency, the maximum amplitudes of mode II pressure disturbances are close to each other for two different frequencies. The locations of peak value expressed in RF are 0.3294 and 0.3255 for $F = 2.2 \times 10^{-4}$ and $F = 1.6 \times 10^{-4}$, respectively. Again, the location of the peak amplitudes expressed in RF are very close in both cases of different frequencies. These results again show that though mode II predicted by the LST is always stable, it can experience growth when it is near the synchronization point with the fast acoustic waves. Such growth does not depend on the frequency very much.

8. Results discussions and conclusions

This paper is the first part of our two-part study on the mechanisms of the receptivity to disturbances of a Mach 4.5 flow over a flat plate by numerical simulations and by linear stability analyses. The main focus of this paper is on stability characteristics of the boundary-layer wave modes and their resonant interactions. These interactions play a critical role in the receptivity process of a supersonic boundary layer. The numerical solutions of both steady base flow and unsteady flow induced by forcing disturbances are obtained by using a fifth-order shock-fitting method of Zhong (1998). While the receptivity mechanisms are mainly studied based on the analyses of the numerical solutions, the wave modes generated in the boundary layer are identified by means of LST. The LST is also used to study the linear stability characteristics and wave synchronization of the wave modes, which play an important role in the receptivity process in the supersonic boundary layer. The results presented in the previous sections are discussed further in this section.

8.1. *Stability characteristics of wave modes*

The linear stability properties of the Mack modes, i.e. the first mode and the second mode, are well understood owing to the in-depth studies by Mack (1984). For the receptivity studies, however, another family of stable normal modes in the supersonic boundary layer play an important role in transferring perturbation energy from the forcing waves to the unstable Mack modes. These stable modes are termed modes I, II, III, etc. in this paper. Though they are linearly stable modes, they can have substantial energy growth in the receptivity process because of their resonant interactions with the forcing acoustic waves. They can also induce the growth of the Mack modes because of their resonant interactions with the Mack modes. Currently, the stability characteristics of these boundary-layer wave modes are not known, though the characteristics of the first and second mode instability are well known. Therefore, the linear stability properties of the normal modes in the supersonic boundary layer are first studied before studying the receptivity of the supersonic boundary layer.

The characteristics of different boundary-layer normal modes, both the Mack modes and the family of stable modes (mode I, mode II, etc.), have been studied first by the LST analysis. For cases of different frequencies and different Reynolds numbers, the results show that the phase velocities (or wavenumbers) of all normal modes in the supersonic boundary layer are functions of the product of non-dimensional frequency and Reynolds number (RF). Almost the same values of RF are obtained for branch I or branch II neutral stability points of the second mode for cases of different frequencies and different Reynolds numbers. Both the family of Mack modes (the first mode and second mode) and the family of stable modes (mode I, mode II, etc.) coexist in the boundary layer. The family of stable wave modes are originated with the same initial phase velocities as the fast acoustic waves. After these wave modes appear, their phase velocities decrease gradually as they propagate downstream. On the other hand, the family of Mack modes are originated from the leading edge with initial phase velocities close to those of slow acoustic waves. For Mack modes, the phase velocities are less than the free-stream velocity, and approach the value of the free-stream velocity as they propagate downstream. It is also found that the conventionally defined first, second and third instability modes in a supersonic boundary layer are, in fact, different sections of the same Mack mode during propagation downstream.

The LST results show that all normal modes are stable except the Mack modes, which are unstable in certain small ranges of RF. However, the stable modes such as modes I and II play an important role in the receptivity process because the phase velocity distributions of the Mack modes intersect with those of the stable modes I, II, etc. as RF increases. At the intersecting points between the phase velocity curves of the Mack modes and the stable modes, the Mack modes are synchronized with modes I, II, III, or higher modes because they have the same frequency and the same phase velocity. In addition, different modes at the synchronization points have almost the same wave structures inside the boundary layer. Therefore, it is impossible to distinguish different modes from their wave structure alone.

8.2. *Simulation of wave mode propagations and resonant interactions*

Extensive unsteady flow simulations have been carried out to study the receptivity of the supersonic boundary layer to various forcing waves. In this paper, the numerical simulation mainly focuses on the studies of the linear wave mode characteristics and their resonant interactions, which are the crucial part of the receptivity process. Two groups of computational cases are studied. The first group concerns the response of supersonic boundary layer to forcing waves of different wave modes imposed at the inlet located near the leading edge. The profiles of the forcing waves at the inlet are obtained from the LST for a given wave mode at a fixed frequency.

The main findings of the numerical simulation studies are the importance of wave resonant interactions which cannot be predicted by the LST analysis. The numerical simulation studies on the propagation of modes I and II show that there are strong resonant interactions between these modes and other waves, including the Mack modes and the acoustic waves. The resonant interactions occur at the locations of wave synchronization points predicted by the LST analysis. The interactions include those between the fast acoustic waves and the stable modes (modes I and II), and those between the stable modes and the Mack modes (the first and second modes). The resonant interactions between the fast acoustic waves and modes I and II lead to the amplification of modes I and II waves, even though both of them are linearly stable. Similarly, both mode I and mode II waves can become synchronized with the Mack modes. As a result, the synchronization between mode I and the Mack modes lead to an energy exchange between the two different modes and excitations of the Mack modes, especially the unstable second mode, in the supersonic boundary layer.

Though the steady base flow is obtained for the adiabatic wall boundary condition, different conditions can be imposed on the temperature perturbation conditions. The effects of wall temperature perturbation conditions on the stability of the wave modes are also studied in this paper. Both the LST and simulation results show that all normal modes of the isothermal cases are more stable than those of the corresponding adiabatic cases. However, the stable modes I and II are not much affected by the changes of wall temperature perturbation conditions. The effects of wave frequency on the propagation of the wave modes have also been studied. It is found that the Mack modes of lower frequencies have higher growth rates and larger downstream movement of branch II neutral stability points. Based on the LST prediction, the locations of branch II neutral stability points of the second mode in terms of RF are the same for cases with different frequencies and different Reynolds numbers.

The numerical solutions also show that the wavenumbers obtained from the numerical simulations agree very well with those predicted by the LST. However, there are significant differences between the growth rates obtained from the numerical simulations and those predicted by the LST. The LST analysis consistently underpredicts the growth rates of the Mack modes. The difference between the growth rates obtained by the numerical solutions and those predicted by the LST may be due to the parallel mean flow assumption used in LST.

8.3. *Conclusions*

To summarize, in addition to the conventional Mack modes, there exist a family of stable wave modes (modes I, II, etc.) in the supersonic boundary layer. These modes play a very important role in the receptivity process of excitation of the unstable Mack modes, especially the second mode. Though mode I and mode II waves are always stable, they can play an important role in the receptivity process because they can have resonant interactions with both the fast acoustic waves and the Mack-mode waves. Such interactions lead to the exchange of energy between the stable modes and the Mack modes to induce the Mack modes in the boundary layer. On the other hand, the stable mode II can also interact with the fast acoustic waves to lead to a substantial amplitude growth of mode II in the boundary layer. Therefore, the stable wave modes such as modes I and II are critical in transferring wave energy between the acoustic waves and the unsteady second mode. It is important for the receptivity study to understand the role of modes I and II in the excitation of the unstable Mack modes.

The results of this paper also point out the critical role of fast acoustic waves as forcing waves in the receptivity process. The forcing acoustic waves can originate from noise in the free-stream. The numerical studies of the receptivity of supersonic boundary layer to free-stream disturbances must account for the interaction of the acoustic waves with the oblique bow shock. Such studies required extensive simulations and analyses; the results will be presented in another paper.

This research was supported by the Air Force Office of Scientific Research, USAF, under AFOSR Grant F49620-00-1-0101. The program manager is Dr John Schmisseur. The views and conclusions contained herein are those of the authors and should not be interpreted as necessarily representing the official policies or endorsements either expressed or implied, of the Air Force Office of Scientific Research or the US Government.

REFERENCES

Arnal, D., Maslov, A. A., Sidorenko, A. & Shiplyuk, A. N. 1999 Experimental investigation of hypersonic boundary layer receptivity to acoustic disturbances. *Fluid Dyn.* **5**, 681–686.

Bayliss, A., Maestrello, L. & Krishnan, R. 1991 On the interaction between first and second-mode waves in a supersonic boundary layer. *Phys. Fluids* A **3**, 3014–3020.

Bertram, M. H. 1958 Boundary-layer displacement effects in air at Mach number of 6.8 and 9.6. *NACA TN* 4133.

Choudhari, M. & Strett, C. L. 1990 Boundary layer receptivity phenomena in three-dimensional and high-speed boundary layers. *AIAA Paper* 90-5258.

Choudhari, M. & Strett, C. L. 1993 Interaction of a high-speed boundary layer with unsteady free-stream disturbances. In *Transitional and Turbulent Compressible Flows* (ed. L. D. Kral & T. A. Zang), pp. 15–28. FED-151, ASME.

Dunn, D. W. & Lin, C. C. 1955 On the stability of the laminar boundary layer in a compressible fluid. *J. Aero. Sci.* **22**, 455–477.

Eissler, W. & Bestek, H. 1996 Wall-temperature effects on transition in supersonic boundary layers investigated by direct numerical simulations. In *Transitional Boundary Layers in Aeronautics* (ed. R. A. W. M. Henkes & J. L. van Ingen), pp. 459–467. North-Holland.

Eissler, W. & Bestek, H. 1996 Spatial numerical simulations of linear and weakly nonlinear instabilities in supersonic boundary layers *Theor. Comput. Fluid Dyn.* **8**, 219–235.

Fedorov, A. V. & Alexander, V. 1997 Laminar turbulent transition in a hypersonic boundary layer: receptivity and instability pre-history. *Final Rep.* NASA-N97-29589.

Fedorov, A. V. & Khokhlov, A. P. 1991 Excitation of unstable modes in a supersonic boundary layer by acoustic waves. *Fluid Dyn.* **4**, 67–74.

Fedorov, A. V. & Khokhlov, A. P. 1992 Sensitivity of a supersonic boundary layer to acoustic disturbances. *Fluid Dyn.* **1**, 40–47.

Fedorov, A. V. & Khokhlov, A. P. 2001 Prehistory of instability in a hypersonic boundary layer. *Theor. Comput. Fluid Dyn.* **14**, 359–375.

Fedorov, A. V. & Khokhlov, A. P. 2002 Receptivity of hypersonic boundary layer to wall disturbances. *Theor. Comput. Fluid Dyn.* **15**, 231–254.

Fezer, A. & Kloker, M. 1999 Transition processes in Mach 6.8 boundary layers at varying temperature conditions investigated by spatial direct numerical simulation. In *Symp. on New Results in Numerical and Experimental Fluid Mechanics II* (ed. W. Nitsche, H.-J. Heinemann & P. Reinhar), pp. 138–145, Notes on Numerical Fluid Mechanics 72. Braunschweig; Wiesbaden: Vieweg.

Fedorov, A. V. & Tumin, A. 2001 Initial-value problem for hypersonic boundary layer flows. *AIAA Paper* 2001-2780.

Goldstein, M. E. & Hultgren, L. S. 1989 Boundary-layer receptivity to long-wave free-stream disturbances. *Annu. Rev. Fluid Mech.* **21**, 137–166.

Hudson, M. L. 1996 Linear stability of hypersonic flows in thermal and chemical nonequilibrium. PhD thesis, North Carolina State University.

Kendall, J. M. 1957 An experimental investigation of leading-edge shock-wave-boundary-layer interaction at Mach 5.8. *J. Aero. Sci.* **24**, 47–56.

Kendall, J. M. 1967 Supersonic boundary-layer stability experiments. In *Proc. Transition Study Group Meeting* (ed. W. D. McCauley), 2(A), Aerospace Corp., San Bernardino.

Kendall, J. M. 1975 Wind tunnel experiments relating to supersonic and hypersonic boundary-layer transition. *AIAA J.* **13**, 290–299.

Kerschen, E. J. 1989 Boundary-layer receptivity. *AIAA Paper* 89-1109.

Kleiser, L., Guo, Y. & Adams, N. A. 1996 Comparison of temporal and spatial direct numerical simulation of compressible boundary-layer transition. *AIAA J.* **34**, 683–690.

Krogmann, P. 1977 An experimental study of boundary-layer transition on a slender cone at Mach 5. In *Symp. on Laminar–Turbulent Transition.* AGARD-CP-224.

Lee, L. & Probstein, R. F. 1952 *Hypersonic Viscous Flow over a Flat Plate.* Princeton University, Aeronautical Engineering Laboratory.

Lin, R., Malik, M. R. & Sengupta, R. 1999 Computation of hypersonic boundary-layer response to external disturbances. *AIAA Paper* 99-0411.

Ma, Y. & Zhong, X. 2000 Direct numerical simulation of instability of nonequilibrium reacting hypersonic boundary layers. *AIAA Paper* 2000-0539.

Ma, Y. & Zhong, X. 2001 Numerical simulation of receptivity and stability of nonequilibrium reacting hypersonic boundary layers. *AIAA Paper* 2001-0892.

Ma, Y. & Zhong, X. 2003 Receptivity of a supersonic boundary layer over a flat plate. Part 2. Receptivity to free-stream sound. *J. Fluid Mech.* **488**, 79–121.

Mack, L. M. 1975 Linear stability theory and the problem of supersonic boundary-layer transition. *AIAA J.* **13**, 278–289.

Mack, L. M. 1984 Boundary layer linear stability theory. In *AGARD Rep.* 709.

Malik, M. R. 1990 Numerical methods for hypersonic boundary-layer stability. *J. Comput. Phys.* **86**, 376–413.

Malik, M. R. 2000 Hypersonic boundary-layer receptivity and stability. In *IUTAM Symp. on Laminar–Turbulent Transition* (ed. H. F. Fasel & W. S. Saric), pp. 409–414. Springer.

Maslov, A. A. & Semionov, N. V. 1986 Excitation of nature oscillations in a boundary layer. *Fluid Dyn.* **3**, 74–78.

MASLOV, A. A., SHIPLYUK, A. N., SIDORENKO, A. & ARNAL, D. 2001 Leading-edge receptivity of a hypersonic boundary layer on a flat plate. *J. Fluid Mech.* **426**, 73–94.

PATE, S. R. 1971 Measurements and correlation of transition Reynolds numbers on sharp slender cones at high speeds. *AIAA J.* **9**, 1082.

PATE, S. R. & SCHUELER, C. J. 1969 Radiated aerodynamic noise effects on boundary-layer transition in supersonic and hypersonic wind tunnels. *AIAA J.* **7**, 450.

POTTER, J. L. 1968 Observations on the influence of ambient pressure on boundary-layer transition. *AIAA J.* **6**, 1907.

POTTER, J. L. & WHITFIELD, J. D. 1962 Effects of slight nose bluntness and roughness on boundary-layer transition in supersonic flows. *J. Fluid Mech.* **12**, 501–535.

PRUETT, C. D. & CHANG, C. L. 1993 A comparison of PSE and DNS for high-speed boundary-layer flows. In *Transitional and Turbulent Compressible Flows* (ed. L. D. Kral & T. A. Zang), pp. 57–67. FED-151, ASME.

PRUETT, C. D., ZANG, T. A., CHANG, C. L. & CARPENTER, M. H. 1995 Spatial direct numerical simulation of high-speed boundary-layer flows, Part I: Algorithmic considerations and validation. *Theor. Comput. Fluid Dyn.* **7**, 49–76.

RESHOTOKO, E. 1990 Panel summary: receptivity. In *Instability and Transition,* vol. 1 (ed. M. Y. Hussaini and R. G. Viogt), pp. 217–232. Springer.

SARIC, W. S., REED, H. L. & KERSCHEN, E. J. 2002 Boundary-layer receptivity to freestream disturbances. *Annu. Rev. Fluid Mech.* **34**, 291–319.

SEMIONOV, N. V., KOSINOV, A. D. & MASLOV, A. A. 1996 Experimental investigation of supersonic boundary-layer receptivity. In *Transitional Boundary Layers in Aeronautics* (ed. R. A. W. M. Henkes & J. L. van Ingen), pp. 413–420. North-Holland.

SEMIONOV, N. V., KOSINOV, A. D. & MASLOV, A. A. 1998 An experimental study of instability disturbances excitation by external source in supersonic boundary layer of a blunt plate. In *Intl Conf. on the Methods of Aerophys. Res. (ICMAR'98), Novosibirsk, Russia*, pp. 192–197.

STETSON, K. F. & KIMMEL, R. L. 1992 On hypersonic boundary layer stability. *AIAA Paper* 92-0737.

STETSON, K. F. & KIMMEL, R. L. 1993 On the breakdown of a hypersonic laminar boundary layer. *AIAA Paper* 93-0896.

STETSON, K. F., THOMPSON, E. R., DONALDSON, J. C. & SILER, L. G. 1986 Laminar boundary layer stability experiments on a cone at Mach 8, Part 4: on unit Reynolds number and environmental effects. *AIAA Paper* 86-1087.

ZHONG, X. & LEE, T. 1996 Nonequilibrium real-gas effects on disturbance/bow shock interaction in hypersonic flow past a cylinder. *AIAA Paper* 96-1856.

ZHONG, X. 1997 Direct numerical simulation of hypersonic boundary-layer transition over blunt leading edges, Part II: Receptivity to sound. *AIAA Paper* 97-0756.

ZHONG, X. 1998 High-order finite-difference schemes for numerical simulation of hypersonic boundary-layer transition. *J. Comput. Phys.* **144**, 662–709.

ZHONG, X. 2001 Leading-edge receptivity to freestream disturbance waves for hypersonic flow over a parabola. *J. Fluid Mech.* **441**, 315–367.